Journal of Marine Systems 77 (2009) 369–387

Contents lists available at ScienceDirect

Journal of Marine Systems

journal homepage: www.elsevier.com/locate/jmarsys

A dense water outflow from the Ross Sea, Antarctica: Mixing and the contribution of tides

Robin Muench [a,*], Laurie Padman [b], Arnold Gordon [c], Alejandro Orsi [d]

[a] Earth & Space Research, 10433 Ravenna Ave NE, Seattle, WA 98125-7745, USA
[b] Earth & Space Research, 3350 SW Cascade Ave., Corvallis, OR 97333, USA
[c] Lamont-Doherty Earth Observatory, Columbia University, Palisades, NY 10964, USA
[d] Texas A&M University, College Station, TX 77845-3146, USA

ARTICLE INFO

Article history:
Received 24 September 2007
Accepted 1 November 2008
Available online 19 November 2008

Keywords:
Dense outflows
Tidal currents
Diapycnal mixing
Antarctic Bottom Water
Ross Sea

ABSTRACT

We use hydrographic, current, and microstructure measurements, and tide-forced ocean models, to estimate benthic and interfacial mixing impacting the evolution of a bottom-trapped outflow of dense shelf water from the Drygalski Trough in the northwestern Ross Sea. During summer 2003 an energetic outflow was observed from the outer shelf (~500 m isobath) to the ~1600 m isobath on the continental slope. Outflow thickness was as great as ~200 m, and mean speeds were ~0.6 m s^{-1} relative to background currents exceeding ~1 m s^{-1} that were primarily tidal in origin. No outflow was detected on the slope in winter 2004, although a thin layer of dense shelf water was present on the outer shelf. When the outflow was well-developed, the estimated benthic stress was of order one Pascal and the bulk Froude number over the upper slope exceeded one. Diapycnal scalar diffusivity (K_z) values in the transition region at the top of the outflow, estimated from Thorpe-scale analysis of potential density and measurements of microscale temperature gradient from sensors attached to the CTD rosette, were of order 10^{-3}–10^{-2} m^2 s^{-1}. For two cases where the upper outflow boundary was particularly sharply defined, entrainment rate w_e was estimated from K_z and bulk outflow parameters to be ~10^{-3} m s^{-1} (~100 m day^{-1}). A tide-forced, three-dimensional primitive equation ocean model with Mellor-Yamada level 2.5 turbulence closure scheme for diapycnal mixing yields results consistent with a significant tidal role in mixing associated with benthic stress and shear within the stratified ocean interior.

1. Introduction

Antarctic Bottom Water (AABW), a major component of the global deep ocean, is produced when cold, dense water formed on the Antarctic continental shelves mixes with Modified Circumpolar Deep Water (MCDW) that, in turn, is derived from offshore Circumpolar Deep Water (CDW) (Whitworth et al., 1998). Sinking and northward spreading of AABW and other dense water types along the Antarctic margins is a significant component of the global meridional overturning circulation (MOC); see, e.g., Johnson (2008). Three source regions around Antarctica are believed to contribute the bulk of AABW: the southwestern and western Weddell Sea; the Adèlie Land Coast near the Mertz Glacier; and, the western Ross Sea (Rintoul, 1998; Baines and Condie, 1998; Gordon, 1998; Orsi et al., 1999; Bindoff et al., 2000; Foldvik et al., 2004; Williams et al., 2008).

The mechanisms that produce the cold, dense source water types over the Antarctic continental shelves are reasonably well understood, albeit difficult to quantitatively model; however, the actual formation process for AABW is less clear. From many previous studies (e.g., Gill, 1973), it appears that the critical mixing processes occur near the shelf break, where shelf water is brought into close proximity with MCDW at the Antarctic Slope Front (ASF).

* Corresponding author. Tel.: +1 206 363 7528.
E-mail addresses: rmuench@esr.org (R. Muench), padman@esr.org (L. Padman), agordon@ldeo.columbia.edu (A. Gordon), aorsi@tamu.edu (A. Orsi).

0924-7963/$ – see front matter © 2008 Elsevier B.V. All rights reserved.
doi:10.1016/j.jmarsys.2008.11.003

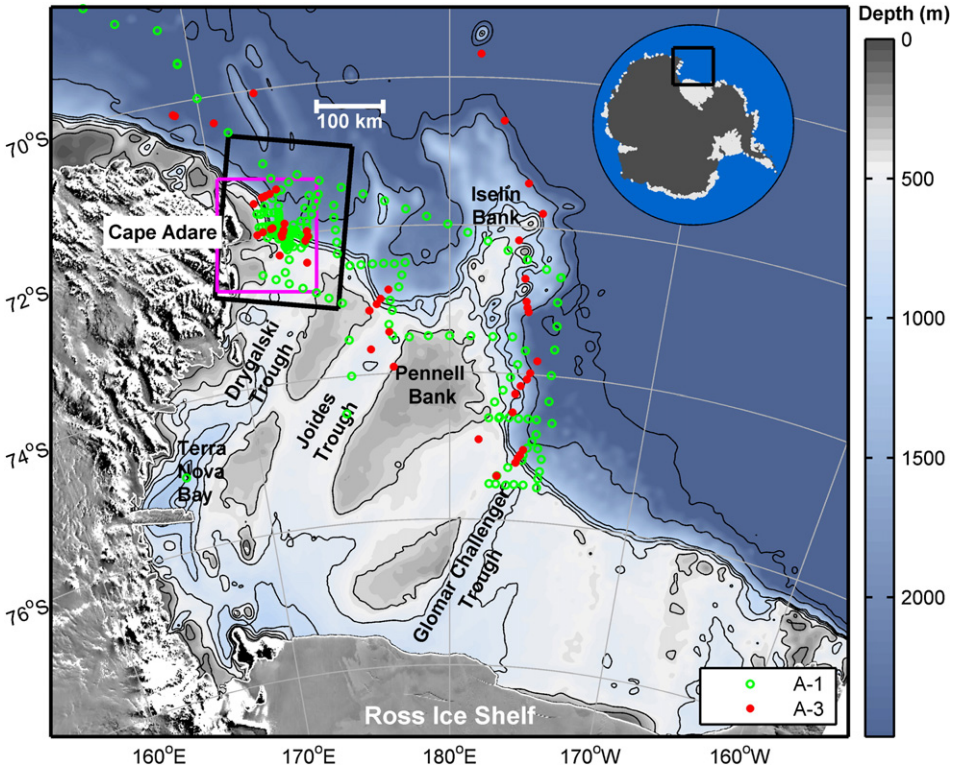

Fig. 1. Bathymetry and location diagram for the northwest Ross Sea continental shelf. Bathymetry is derived from a 2007 update to ETOPO2 (pers. comm., D. Sandwell, 2007). AnSlope 1 and AnSlope 3 CTD stations are shown by green circles and red dots, respectively. The magenta rectangle shows the area surrounding the Drygalski Trough sill (see Fig. 2). The black rectangle shows the domain of the tide-forced, three-dimensional high-resolution numerical model described by Padman et al. (2008).

The shelf break is a complex region, however, with several advection and mixing processes occurring concurrently. Our ability to adequately model the hydrographic properties and cross-slope fluxes depends on first identifying all the potentially relevant processes, then being able to quantify the contribution of each process to the total water mass conversion and export.

The Antarctic Slope (AnSlope) project (Gordon et al., 2004, 2008) was initiated in 2003 to advance our understanding of cross-slope water mass exchange processes and mixing along the shelf break. The project obtained data from the northwestern Ross Sea (Fig. 1), with most effort concentrated near the sill at the northern end of the Drygalski Trough (Fig. 2). This region was chosen for the presence of all major features that we wished to study including a known, if poorly quantified, outflow of High Salinity Shelf Water (HSSW) across the Drygalski Trough sill (Jacobs et al., 1970; Locarnini, 1994), a well developed slope front, and strong tidal currents (Padman et al., 2002, 2003; Erofeeva et al., 2005).

The AnSlope data sets revealed an energetic, bottom-trapped flow of dense water flowing north across the Drygalski Trough sill then down the continental slope (Gordon et al., 2004, 2008). The outflow was identifiable, through deep temperature and salinity anomalies, at least as far as the central slope (~1600 m depth) offshore Cape Adare, about 50 km to the northwest of the sill (Figs. 1, 2 and 3). The outflow was observed during two AnSlope cruises in the austral summers of 2003 and 2004 but not during a cruise in late winter 2004. Outflow velocities, measured with a lowered acoustic Doppler current profiler (LADCP), sometimes approached 2 m s^{-1} (Visbeck and Thurnherr, 2008). The mean outflow velocities were ~0.4–0.6 m s^{-1} (Gordon et al., 2004, 2008). In the summer 2003 cruise, the estimated total outflow transport near Cape Adare was ~1.7–2.6 Sv, of which ~0.5–0.8 Sv was a type of HSSW referred to as western Ross Sea shelf water (Gordon et al., 2004). The descent angle of the outflow, from both the LADCP profiles and moored current meter records, was ~35° relative to the local isobaths (Gordon et al., 2004, 2008). This value is significantly higher than "canonical" descent angles of order 10° (e.g., Killworth, 1977).

The downstream changes in outflow hydrographic properties in the summer 2003 cruise data set suggest that, by the time the outflow passed Cape Adare, its volume flux had increased by a factor of ~3–4 relative to the flux of HSSW at the Drygalski Trough sill ~50 km to the southeast. The implied advection time along this path, assuming the typical outflow speed was ~0.6 m s^{-1}, is ~1 day. If we interpret the flux increase as being caused entirely by entrainment of overlying intermediate water, we infer an entrainment rate w_e of ~2–4 mm s^{-1} (~200–400 m day^{-1}), implying that the interface above the outflow was actively mixing. To date, however, AnSlope analyses have not demonstrated that the turbulence required to drive the inferred entrainment was actually occurring. Alternative hypotheses include dilution of the outflow by lateral (isopycnal) mixing, and the possibility that the outflow water found offshore Cape Adare did not

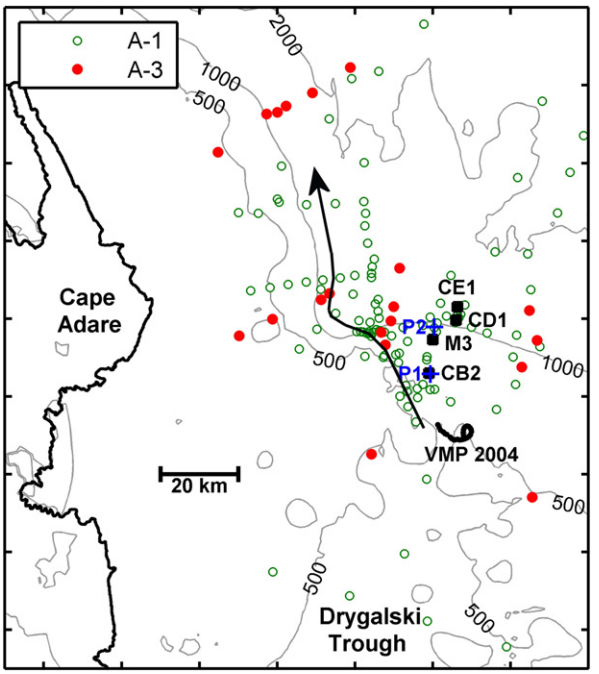

Fig. 2. Close-up of area surrounding the Drygalski Trough sill (magenta rectangle on Fig. 1). Green circles and red dots show AnSlope 1 and AnSlope 3 CTD stations, respectively. Black contours show isobaths. Locations of moorings CB2, CD1 and CE1 (2003/04), and mooring M3 (2004/05) are indicated by black squares. Locations of profiles for VMP yo-yo time series in 2004 (VMP 2004) are indicated. Locations of model grid points P1 (near CB2) and P2 (north of M3) are shown as blue '+' symbols. The approximate path of the outflow during AnSlope 1 (austral summer 2003) is indicated.

originate at the assumed source at the Drygalski Trough sill. The plausibility of the latter hypothesis rests on the non-synoptic nature of the surveys, and the coarse station spacing (both along- and cross-slope) relative to the length scales of other energetic processes occurring along the shelf break and upper slope, as explained below.

The difficulty of sampling in this environment was highlighted by Gordon et al. (2004), who described energetic "pulsing" of downslope flow of almost pure HSSW observed near the seabed at mooring CE1 on the mid-slope (~1400 m water depth) north of the sill (see Fig. 2 for mooring location). These pulses, which were each observed at CE1 for only a few hours, were associated with strong tidal currents during periods of spring tides. Barotropic tide models for the region, including one assimilating vessel-mounted acoustic Doppler current profiler (VMADCP) data from the first AnSlope cruise (Erofeeva et al., 2005), indicate that peak cross-slope tidal currents can exceed 1 m s^{-1} along this section of the shelf break. Thus, at least during spring tides, most kinetic energy is associated with tides rather than the outflow's intrinsic dynamics.

Energetic tidal currents not only contribute to cross-slope transport of the outflow, but also to benthic mixing. Whitworth and Orsi (2006) reported, from their analyses of time series data from moorings, that benthic-layer hydrographic properties over the shelf near the Drygalski Trough sill changed dramatically through a spring-neap tidal cycle. The benthic layer at neap tides was thin, and composed of relatively pure HSSW. In contrast, at spring tides, the benthic layer varied on tidal time scales, was often hundreds of meters thick, and was composed of a mixture of HSSW and MCDW.

We conclude from these studies that both advection and mixing of the benthic outflow of dense water from the Drygalski Trough are modulated by tides. We do not, however, know the extent to which tides contribute to the *mean* outflow path or the *mean* hydrographic properties and flux of the outflow. That is, are tides merely unwelcome "noise" in our data, or must tides be represented explicitly in models that attempt to quantify the Antarctic contribution to the global MOC? Furthermore, while stirring of the benthic layer is undoubtedly increased by the addition of tides, we do not yet know whether tides contribute significantly to the mean rate of entrainment at the upper edge of the outflow. Nor do we even know whether diapycnal mixing between the outflow and the overlying ambient water is sufficiently energetic to explain the observed rapid downstream dilution of the outflow and the increase in volume transport.

In this paper we address some of these issues by using hydrographic and microstructure data obtained during two of the AnSlope cruises to estimate mixing of the bottom-trapped dense water by benthic and interfacial stresses. These data analyses are supported by results from a tide-forced three-dimensional ocean model (Padman et al., 2008). As will be explained below, for a variety of reasons the available data are not ideally suited to the problem at hand. Nevertheless, the combination of several data sets and comparisons with the model strongly support the hypothesis that (i) the transition region at the top of the benthic layer is actively mixing, and (ii) the tide plays a critical role in setting the mean hydrographic characteristics and flux of the outflow.

2. The field program

2.1. Ship-based vertical profiles of hydrography and currents

The data reported herein were obtained from two of the AnSlope cruises on the RVIB *Nathaniel B. Palmer*; during the austral summer of 2003 (cruise NBP03-02) and the austral winter of 2004 (NBP04-08). Hydrographic data were obtained with a pumped Sea-Bird SBE 911^{+} Conductivity (C), Temperature (T) and Depth (as pressure P) (CTD) profiler. The values of C, T and P were acquired at 24 samples per second. Potential temperature (θ) and salinity (S) were calculated from C, T and P. The C and T values were first edited for obvious spikes such as those due to biota pumped into the sensors, then corrected for time lag and thermal mass effects to minimize spikes in S and potential density σ_{ref}. The choice of reference pressure for potential density depends on our application but is usually chosen as 600 hPa, corresponding approximately to the depth of the shelf break. We denote this value as σ_{600}. This reference is chosen to minimize the potential contribution of thermobaricity to the stability of the water column as represented by the vertical gradient of σ_{ref} (z). Station locations are shown in Figs. 1–3.

Most CTD profiles were obtained while the ship was in the pack ice well away from the ice edge, so that no discernible wave motion was affecting the ship. Under these conditions it

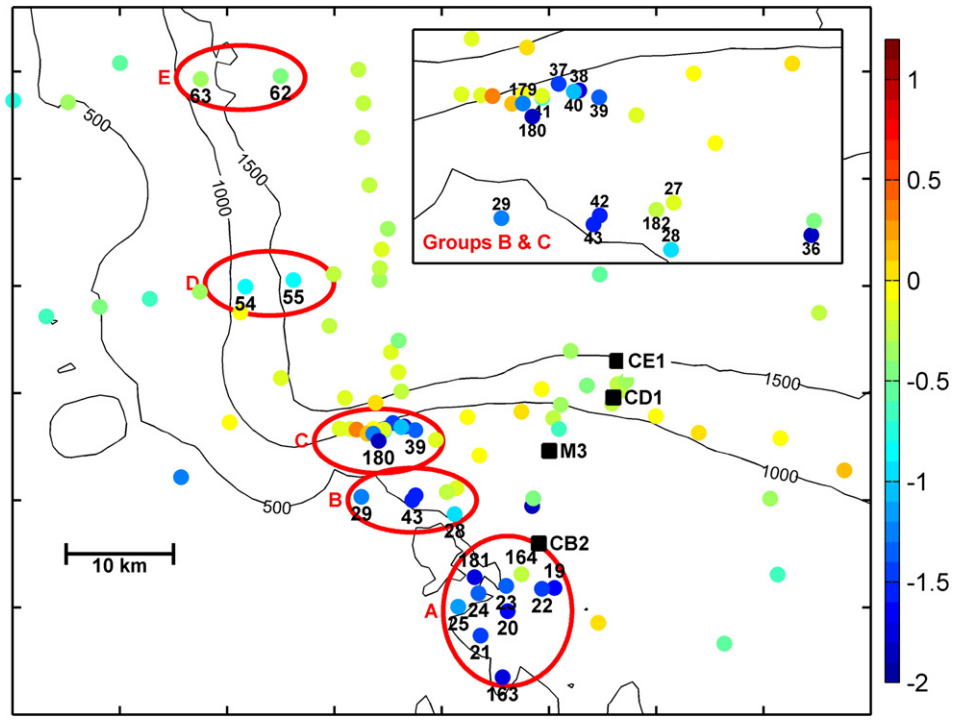

Fig. 3. AnSlope 1 (summer 2003) CTD stations, color-coded by bottom potential temperature θ_b (color scale on right). Red ellipses highlight groups of CTD stations referred to in the text. The 500, 1000, and 1500 m isobaths are indicated. Locations of moorings discussed in text are shown with black squares. Groups B and C are expanded in upper right inset.

is possible to lower the CTD at a nearly constant rate through the water column: a typical descent rate was $w_{CTD} \approx 0.8$ m s^{-1}, with a standard deviation of $\sigma(w_{CTD}) \approx 0.02$ m s^{-1}. For sections of profile for which w_{CTD} was nearly constant, despiking and careful corrections for time lag and thermal mass resulted in high quality measurements having vertical resolution of $dz = 0.25$ m.

Vertical profiles of velocity $u(z) = u(z)i + v(z)j$ were measured concurrently with the CTD profiles using a lowered acoustic Doppler current profiler (LADCP) mounted on the CTD rosette frame. The LADCP consisted of two RDI Workhorse WH300 ADCP heads mounted in an upward–downward looking "Janus" configuration. The resulting current profiles were combined with CTD, GPS and vessel-mounted ADCP (VMADCP) bottom-track data (where available) to produce profiles of absolute velocity with an estimated vertical resolution of ~20 m (~100 m wavelength: cf. Polzin et al., 2002). Typical velocity errors at this resolution are ~0.05 m s^{-1}. For more information on the LADCP, see Visbeck and Thurnherr (2008).

Some ocean velocity data were also obtained from the 150 kHz narrow-band VMADCP; however, this instrument provided useful data only for short periods while the ship was stopped on a station. Data could not be acquired while the ship was underway in ice, and some data were also lost on-station due to cavitation from the thrusters used to maintain ship position relative to surrounding ice floes.

The CTD/LADCP stations during summer 2003 included multiple stations over the sill and adjacent upper slope, and several cross-slope transects up to ~50 km downstream of the sill, just east of Cape Adare (Fig. 2). Due to weather and logistical constraints, far fewer profiles were measured in winter 2004 than during summer 2003. These data are not reviewed in detail herein, since no energetic benthic outflow was observed during this cruise.

2.2. Mooring measurements of hydrography and currents

Moorings were deployed over the Drygalski Trough sill and adjacent slope in early 2003 and recovered in early 2004 (Whitworth and Orsi, 2006). Moorings were again deployed, but at new locations, on the same 2004 cruise and recovered in early 2005. Time series of *T*, *S*, *P* and *u* were obtained at several depths on each mooring. Gordon et al. (2008) provide a complete review of the AnSlope mooring records.

Most moorings experienced significant, and in some instances extreme, blow-down due to line drag from the strong currents; see Fig. 4 of Padman et al. (2008). The pressure time series allow us, however, to determine record intervals suitable for analyses. Deep current records on the mid and upper slope moorings were judged unreliable during spring tides because of the potential for instrument tilt to impact the speed rotor response (Gordon et al., 2008); hence, we use only scalar variables in our analyses. Locations of moorings cited herein are shown on Fig. 2.

2.3. CTD-mounted microstructure profiling

In AnSlope 1 (summer 2003) we deployed a CTD-mounted Microstructure Profiling System (CMiPS), manufactured by

Table 1
Outflow properties for the summer 2003 CTD profiles within the five groups shown in Fig. 3.

CTD	Group	θ_b	S_b	H_b (m)	$\langle\theta\rangle_b$	$\langle S\rangle_b$	$\delta\sigma_{ref}$	δu (m s^{-1})	Spring-neap phase	δ^x_{tide}(km)	R_{SW} (%)
19	A	−1.70	34.77	281	−1.22	34.713	0.11	0.49	Falling	8.6	87
20	A	−1.68	34.77	367	−1.09	34.670	0.10	0.35	Falling	7.7	85
21	A	−1.55	34.76	385	−1.02	34.661	0.10	0.20	Falling	6.2	78
22	A	−1.47	34.76	126	−0.81	34.731	0.11	0.32	Falling	8.4	73
23	A	−1.45	34.76	136	−0.77	34.730	0.11	0.26	Falling	6.9	72
24	A	−1.40	34.76	142	−0.85	34.732	0.12	0.26	Falling	6.2	70
25	A	−1.24	34.75	102	−0.90	34.731	0.10	0.20	Falling	5.2	61
163	A	−1.80	34.73	81	−1.43	34.716	0.11	0.26	Rising	3.7	81 (f)
181	A	−1.78	34.78	137	−1.28	34.750	0.16	0.17	Spring	4.4	52
28	B	−1.03	34.74	110	−0.88	34.734	0.10	0.11	Falling	3.7	64
29	B	−1.33	34.75	113	−1.23	34.740	0.15	0.47	Falling	5.0	98
36	B	−1.89	34.79	342	−1.10	34.671	0.10	0.17	Falling	1.4	35
41	B	−0.7	34.72	75	−0.48	34.708	0.12	0.09	Falling	2.0	35
43	B	−1.63	34.78	68	−1.10	34.749	0.12	0.17	Falling	−0.6	88
182	B	−0.32	34.70	104	−0.28	34.696	0.10	0.17	Spring	2.5	12
37	Ca	−1.32	34.70	208	−1.35	34.709	0.11	0.75	Falling	1.7	51 (f)
38	Ca	−1.82	34.74	88	−1.53	34.711	0.08	0.68	Falling	2.5	93 (f)
39	Ca	−1.24	34.74	96	−0.76	34.719	0.07	0.48	Falling	2.6	58
40	Ca	−1.07	34.74	77	−0.70	34.718	0.07	0.54	Falling	2.4	54
179	Cb	−1.31	34.71	260	−1.25	34.700	0.24	0.45	Spring	6.8	51 (f)
180	Cb	−1.87	34.74	253	−1.46	34.714	0.21	0.74	Spring	9.2	95 (f)
54	D	−0.94	34.72	147	−0.63	34.716	0.06	0.39	Neap	0.7	40
55	D	−0.93	34.72	364	−0.52	34.704	0.05	0.53	Neap	0.4	40
62	E	−0.62	34.71	389	−0.38	34.695	0.05	0.24	Neap	−0.3	28
63	E	−0.51	34.71	484	−0.44	34.707	0.04	0.36	Neap	−0.2	23

Potential temperature and salinity at the bottom of each profile (θ_b and S_b, respectively); thickness of benthic layer including interface (H_b); depth-averaged benthic layer potential temperature and salinity ($\langle\theta\rangle_b$ and $\langle S\rangle_b$, respectively); density and velocity differences between outflow and overlying water, $\delta\sigma_{ref}$ and δu; time of the profile through the spring-neap cycle; cross-slope displacement at the time of each profile (δ^x_{tide}) based on integration of velocity from the Erofeeva et al. (2005) barotropic tide model; and the fraction of shelf water in the bottom water, R_{SW}, are tabulated. Stations with a "low salinity" shelf water source ("fHSSW": see text for details) are indicted by '(f)' in the last column.

Rockland Scientific, International (RSI). The CMiPS was mounted outboard on the CTD rosette frame with its sensors approximately level with the intake for the pumped Sea-Bird *T* and *C* sensors. The CMiPS was developed in an attempt to obtain scalar microstructure at depths that are not attainable with tethered free-falling microstructure profiler systems and with no increase in time spent on station, since CMiPS samples concurrently with the CTD and LADCP. The instrument measured vertical profiles of *T* and *C* using two rapid-response FP-07 thermistors and a Sea-Bird SBE7 microconductivity probe. Instrument motion was monitored with a pressure sensor and a three-axis accelerometer. The *T* and *C* signals from CMiPS were calibrated against CTD data for each profile. The signals were oversampled at 512 Hz to improve data quality after post-processing. The vertical resolution of the thermistors is determined by the CTD descent rate, which was typically $w_{CTD} \approx 0.8$ m s^{-1}. This rate is a compromise between several factors. The FP07 thermistors can only fully resolve the Batchelor wave number scalar spectrum of well-developed turbulence at speeds of order 0.1–0.2 m s^{-1}. At low values of w_{CTD}, however, the angle at which the CTD descends relative to the mean CTD-relative ocean velocity decreases, increasing the likelihood that eddies shed by the CTD rosette frame will contaminate the scalar microstructure signals. Low descent rates were also inconsistent with the primary AnSlope program goal of sampling hydrography and velocity to near the seabed, at many closely spaced stations, within a time frame set by logistical considerations.

As will be shown in Section 3, the CMiPS data acquired during AnSlope 1 proved useful for estimating diapycnal mixing rates; however, interpretation of these results requires caution under some conditions. By measuring only scalars, CMiPS performs poorly in nearly homogenous regions such as the surface mixed and benthic layers. Finescale scalar data are also likely to be contaminated during periods when the supporting CTD rosette frame was significantly tilted or being dragged rapidly through the ocean (Visbeck and Thurnherr, 2008). Data were assumed to be valid only when the descent rate was maintained uniform, and data were not analyzed for $w_{CTD} < 0.5$ m s^{-1}.

2.4. Tethered, free-fall microstructure profiling

In winter 2004 we deployed a tethered, free-falling vertical microstructure profiler (VMP), also manufactured by RSI. This profiler had a maximum profiling depth of 800–1000 m and a descent speed of ~0.7 m s^{-1}. Instrument motion was monitored by a fast-response pressure sensor and three-axis accelerometer. The VMP measured scalar (*T* and *C*) microstructure with sensors similar to those on CMiPS, and shear microstructure with a pair of airfoil shear probes manufactured by RSI. The estimated noise level for the dissipation rate ε based on shear probe data in quiet sections of the water column was $\varepsilon_{noise} \approx 1\text{–}2 \times 10^{-10}$ m^2 s^{-3}. Logistical issues severely limited the time available in the primary study area; hence, the VMP microstructure data in 2004 covered just a single 26-hour time series of ~hourly profiles just north of the Drygalski Trough sill (see Fig. 2 for profiling locations). The

measurements did not coincide with spring tides or with the presence of an energetic outflow; however, they do provide at least indirect information on the processes of interest to the present study.

3. Results

Results from summer 2003 and winter 2004 are treated separately in this section because oceanic conditions differed dramatically between the two periods. An easily identified, dense downslope outflow was seen on the continental slope in summer 2003 (Gordon et al., 2004, 2008) but not in winter 2004. In addition, the summer 2003 data were acquired primarily during spring tides, whereas the winter 2004 data were acquired during neap tides. It is possible that absence of a dense outflow on the slope in the winter cruise is related to phase within the spring-neap cycle; see Padman et al. (2008). There are, however, significant seasonal cycles of atmospheric forcing, sea-ice properties, and dense-water production rates over the shelf, all of which may influence the offshore flux of dense water. These non-tidal influences are topics of separate ongoing analyses and will not be further addressed here.

3.1. Outflow characteristics: summer 2003

The approximate path of the dense outflow during the austral summer 2003 cruise was identified from the distribution of potential temperature θ_b and salinity S_b at the bottom of each CTD cast, typically 5–10 m above the seabed (Fig. 3). We consider the outflow path to be approximate because the station spacing along the two northern cross-slope CTD transects was coarse, and tidal advection of hydrographic features (see Padman et al., 2008) is aliased into the cross-slope transects that took of order one day to complete. The coldest water found near the seabed in the study region had $\theta_b \approx -1.9$ °C, close to the freezing point at surface pressure $T_f(P=0)$ for a typical value of $S_b = 34.7$. The highest measured S_b was ~34.79.

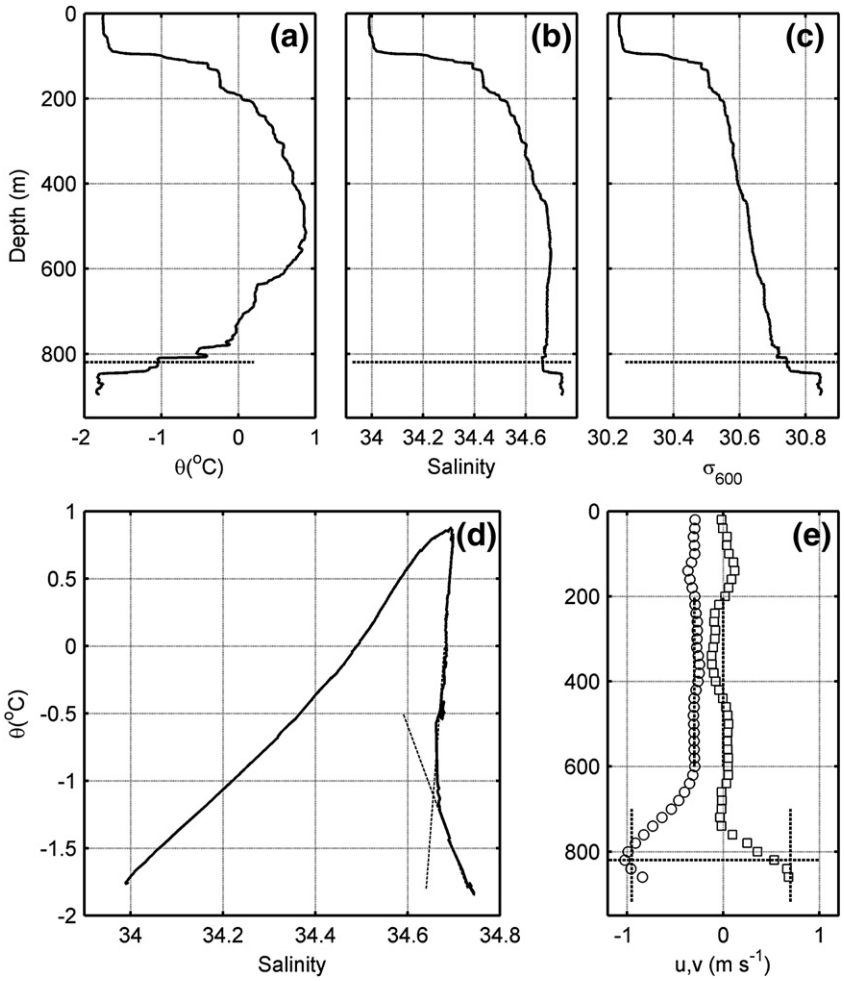

Fig. 4. Example of methodology for determining outflow parameters, applied to CTD 38 (Group Ca). (a)–(c) Vertical profiles of potential temperature θ, salinity *S*, and potential density referenced to 600 hPa (σ_{600}). (d) θ–*S* diagram. (e) Profiles of *u* (○) and *v* (□) components of velocity from LADCP. Initial determination of the top of the outflow at H_b m above the seabed is based on finding the inflexion point in the θ–*S* plot: intersection of dashed lines in (d). This depth is shown as dashed horizontal lines on (a)–(c) and (e). The density difference associated with the outflow is the difference between bottom density and density at H_b m above the seabed. The velocity difference δu between the outflow and the overlying fluid is the difference between the average velocity in the outflow and the average of the mid-water column. These values for each velocity component are shown as vertical dashed lines on (e).

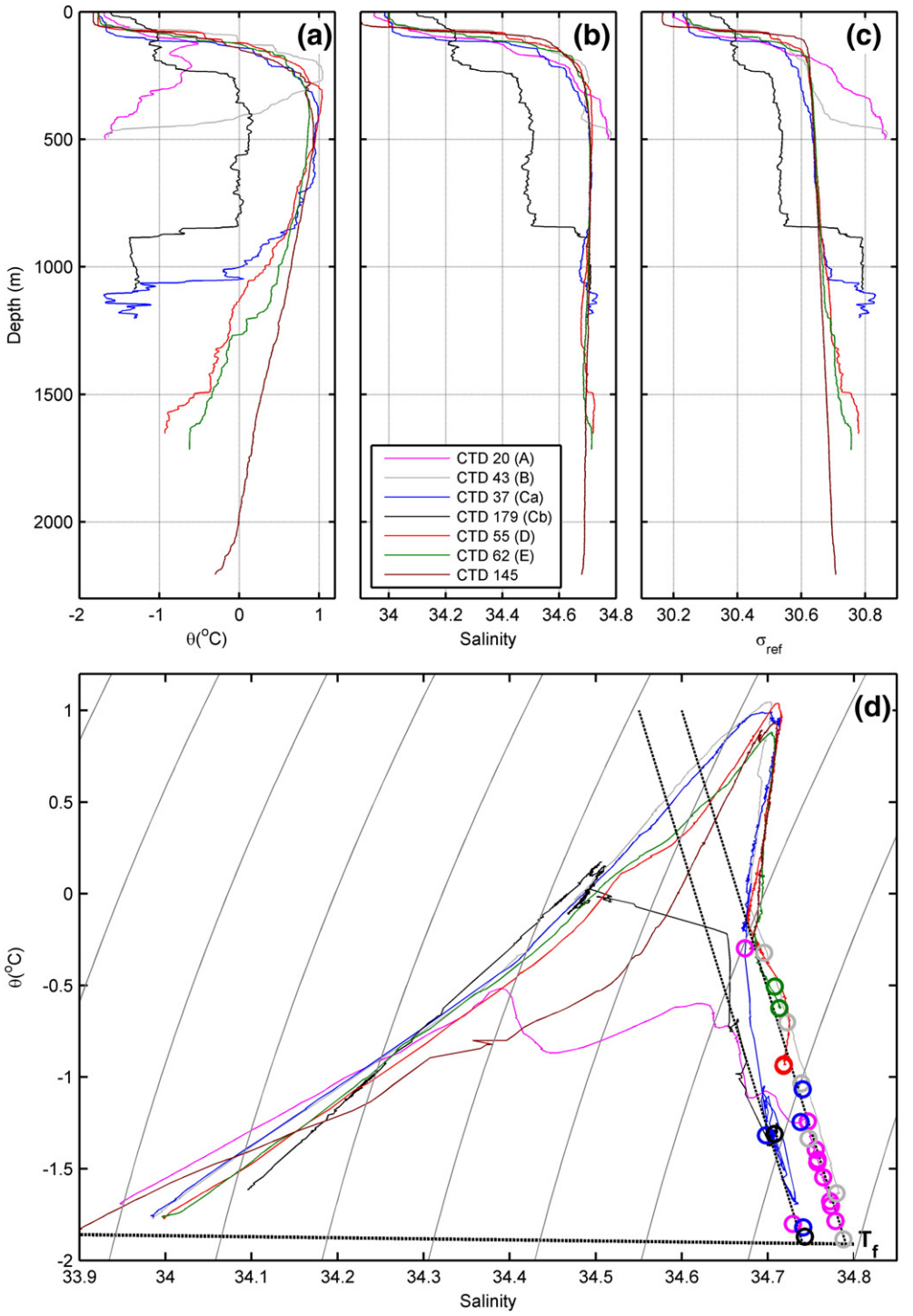

Fig. 5. Profiles of (a) potential temperature $\theta(z)$, (b) salinity $S(z)$ and (c) potential density referenced to 600 hPa, $\sigma_{600}(z)$, for stations representing each of the groups shown in Fig. 3 plus an "offshore" station, CTD 145. Stations and the groups that they represent are identified by legend in panel (b). (d) The same CTD stations shown as $\theta(S)$. Lower black dashed line shows the freezing temperature for surface pressure, T_f. Gray contours show isolines of σ_{600}. Circles show (θ_b,S_b) for all 26 "outflow" stations from the AnSlope summer 2003 cruise. Color coding is by group as indicated in legend in (b). The two black dashed lines represent mixing paths involving "fresh" and "salty" forms of HSSW (fHSSW and sHSSW, respectively).

From maps of θ_b (Fig. 3) and S_b (not shown), and other characterizations (see text below), we identified 25 CTD stations that displayed clear evidence of a dense benthic outflow originating from an HSSW source. Outflow properties for each of these stations are presented in Table 1. In order to determine "bulk" characteristics of the outflow, we defined an

upper "outflow boundary" at H_b above the seabed based primarily on the inflection in the θ–S relationship but also using vertical gradients of $\theta(z)$, $S(z)$ and $u(z)$ in the CTD/LADCP profiles (Fig. 4). We then calculated outflow-averaged values $\langle\theta\rangle_b$ and $\langle S\rangle_b$, where the brackets denote vertical averaging of $\theta(z)$ and $S(z)$ from the bottom of the CTD profile to the outflow boundary.

The bulk velocity and density anomalies of the outflow, δu and $\delta\sigma_{ref}$ respectively, are defined, similarly to Gordon et al. (2004), as the difference between depth-averaged values of u and σ_{600} below the defined boundary and the average of the mid-water column values intended to represent the background "barotropic" flow. The sheared layer above 800 m in the example station shown in Fig. 4e is not associated with a specific density structure (Fig. 4c) but is reminiscent of the tidal-frequency "jets" seen above the seabed over the upper slope in model results presented by Padman et al. (2008), their Fig. 9. This observation highlights the difficulty of interpreting LADCP profiles solely in terms of outflow properties when other sources of significant shear are present.

The stage of the tide during occupation of each station (Table 1) is represented by the approximate phase within the spring-neap cycle and the cross-slope displacement by barotropic tides, δ^x_{tide}, evaluated as the time-integral of cross-slope tidal current derived from the model described by Erofeeva et al. (2005).

The 25 outflow stations have been sorted into five geographically distinct groups, denoted A–E, along the outflow path. Group C, from the upper slope, was divided into two subgroups Ca and Cb based on the profiles' approximate acquisition times. Example profiles of $\theta(z)$, $S(z)$ and $\sigma_{600}(z)$ for each group are shown in Fig. 5.

The example "sill" station 20 (Group A) has HSSW (with $\theta_b \approx T_f(P=0) \approx -1.9$ °C) at the seabed overlain by cool ($\theta_{max} < -0.5$ °C) MCDW. The outer-shelf station 43 (Group B), has the same bottom water properties as station 20, but the intermediate water is almost pure CDW ($\theta_{max} \approx 1.0$ °C) from offshore. Upper slope stations 37 and 179 (Groups Ca and Cb, respectively) have thick, very cold benthic layers. These stations will be discussed in more detail below. Mid-slope stations 55 (Group D) and 62 (Group E) still show the cool and salty benthic layers, but the bulk of each profile is comparable to the offshore deep oceanic hydrography represented by station 145. The coldest bottom water in Groups D and E was $\theta_b \approx -0.9$ °C and -0.6 °C, respectively.

Stations 37 (Group Ca) and 179 (Group Cb) have thick benthic layers capped by sharp (<50 m thick) interfaces. Most other outflow stations have relatively thin, dense benthic layers capped by thick (~200 m) transition regions in which the fraction of pure outflow fluid decreases gradually toward zero at the upper limit of the transition. The latter conditions were similar to those reported for the Red Sea outflow by Peters and Johns (2005).

The parameter pairs (θ_b, S_b) for the 25 selected stations fall on two distinct mixing lines (Fig. 5d); see, also, Gordon et al. (2004, 2008). Twenty of 25 stations fall on the θ–S line representing mixing between HSSW with (θ, S) ≈ (−1.9 °C, 34.79) and LCDW with (θ, S) ≈ (−0.2 °C, 34.68). The remaining stations (stations 37, 38, 163, 179, and 180) fall on a θ–S line representing mixing between slightly fresher HSSW, (θ, S) ≈ (−1.9 °C, 34.74) and LCDW with (θ, S) ≈ (−0.6 °C, 34.65). We refer to the saltier and fresher HSSW source water types as sHSSW and fHSSW, respectively. Following the procedure described by Gordon et al. (2004), we define the fraction of shelf water in the bottom water for each profile (see Table 1). This fraction varies from almost 100% at some stations over the inner and outer sill to ~25% at Group E, consistent with the entrainment rates reported by Gordon et al. (2004).

For each of the variables describing benthic layer properties, we calculated averaged and extreme values for each group (Table 2). These values provide information on the downstream evolution of the outflow; e.g., the trends of increasing outflow thickness H_b and decreasing fraction of shelf water $\langle R_{SW}\rangle$.

We are particularly interested in the stability of the benthic layer as a guide to the potential for mixing between the outflow and the overlying fluid. The static stability is quantified by $\langle\delta\sigma_{600}\rangle$; this value generally decreases downstream, although the greatest values are associated with Group Cb. The dynamic stability of a layered flow can be characterized by the Froude number, *Fr*. Following Holland et al. (2002), we define *Fr* for the transition region at the top of the dense outflow as:

$$Fr = \left(\left(\rho_o \delta u^2\right) / \left(g H_b \delta\sigma_{ref}\right)\right)^{1/2}, \quad (1)$$

where ρ_0 is the fluid density and g is acceleration of gravity. This equation is the functional equivalent of that used by Legg et al. (2009) for computation of *Fr*. Formally, $Fr > 1$ indicates supercritical shear flow, in which breaking interfacial internal waves contribute to turbulent mixing across the transition region. In a more complex flow with sources of shear and density variability at unresolved time and space scales (e.g., baroclinic tides and higher-frequency internal gravity waves), the value of *Fr* based on resolved flow characteristics only provides a guide to the dynamic stability of the flow.

The largest group-averaged value of *Fr* (Table 2) was found for Group Ca ($Fr \approx 1.8$), the earlier of the two sets of stations on the upper slope. This large value implies supercritical flow and vigorous interfacial mixing. Lower values of $Fr = 0.6$ and 0.4 were obtained at Group B (outer shelf) and Group E (farther downslope), respectively, while $Fr \sim 1.3$ for Group D. This bulk representation of outflow stability suggests that mixing will be most vigorous over the upper and central slope, decreasing as the outflow approaches the mid-slope.

3.2. Mixing and entrainment at the upper outflow boundary: summer 2003

High quality measurements of oceanic turbulence were not available during the AnSlope I cruise in summer 2003, when the density outflow was observed on the continental slope. Instead, we characterize the mixing through the transition region at the top of the density outflow using "Thorpe" analysis applied to CTD data, and by interpretation of temperature gradient ($\theta_z = \partial\theta/\partial z$) data from the CTD-mounted Microstructure Profiling System (CMiPS). Neither approach is ideal, but we shall show that they provide generally consistent mixing values.

Thorpe (1977) reordering involves sorting the measured vertical profile of discrete potential density values into a statically stable profile: i.e., one that monotonically increases with depth. The magnitude of the "Thorpe" displacements (the distance that each water parcel must be moved vertically

Table 2
Average bulk outflow properties for summer 2003 profile Groups B–E (Fig. 3).

	Group B	Group Ca	Group Cb	Group D	Group E
CTD profiles	28,29,36,41,43	37–40	179,180	54–55	62–63
H_b (m)	110	160	270	340	610
T_b^{min} (°C)	−1.87	−1.80	−1.85	−0.90	−0.62
S_b^{max}	34.79	34.74	34.745	34.72	34.714
$\langle\theta\rangle_b$ (°C)	−1.046	−0.818	−1.306	−0.379	−0.284
$\langle S\rangle_b$	34.730	34.706	34.705	34.706	34.701
$\langle R_{SW}\rangle$	0.55	0.43	0.69	0.20	0.15
$\lvert u_{barot}\rvert$ (m s^{-1})	0.45	0.30	0.44	0.07	0.25
$\langle\delta\sigma_{ref}\rangle$ (kg m^{-3})	0.12	0.081	0.23	0.057	0.060
$\langle\delta u\rangle$ (m s^{-1})	0.20	0.61	0.60	0.54	0.26
$\langle Fr\rangle$	0.56	1.75	0.74	1.29	0.43
K_z^{Th} (m^2 s^{-1})	0.002	0.05	0.07	0.008	0.01
K_z^{O-C}(m^2 s^{-1})	0.002	0.009	0.05	0.007	0.01

Group C (upper slope) has been broken into two sub-groups (Ca and Cb) based on station occupation time. Tabulated properties are: outflow thickness, H_b, minimum outflow potential temperature and maximum salinity at each group, T_b^{min} and S_b^{max}; ensemble-mean, vertically averaged potential temperature and salinity, $\langle\theta\rangle_b$ and $\langle S\rangle_b$; fraction of shelf water, $\theta = T_f$ ($P=0$), assuming mixing with ambient deep water with (θ, S) = (0 °C, 34.68), $\langle R_{SW}\rangle$, mean barotropic current speed, $\lvert u_{barot}\rvert$; mean outflow-averaged potential density and velocity anomalies, $\langle\delta\sigma_{ref}\rangle$ and $\langle\delta u\rangle$; mean bulk Froude number, Fr from Eq. (1); mean transition layer eddy diffusivity K_z^{Th} based on Thorpe reordering of density; and mean diffusivity in the transition layer, K_z^{O-C} from Eq. (2).

to create the sorted profile) will depend on the turbulent kinetic energy and the buoyancy gradient against which the turbulence is working. Dillon (1982) and many subsequent studies have found that, on average, the root-mean-square (rms) Thorpe displacement (L_{Th}) for an actively mixing patch is given by $L_{Th} \approx 0.8^{-1} L_O$, where $L_O = (\varepsilon/N^3)^{1/2}$ is the Ozmidov length scale, ε (m^2 s^{-3}) is the dissipation rate of turbulent kinetic energy and N is the characteristic buoyancy frequency (s^{-1}) after reordering. Once L_O and ε have been estimated from measured L_{Th} via these relationships, scalar diffusivity can be obtained as $K_z = \Gamma\varepsilon/N^2$ (Osborn 1980), where a typical value of the mixing efficiency Γ is ~0.2 (Gregg, 1987).

The Thorpe analysis procedure was applied to profiles of σ_{600} obtained from $T(z)$ and $S(z)$ from the CTD at depth increments of $dz = 0.25$ m (see Section 2.1). Oceanic turbulence is highly variable in space and time; hence, it is not possible to make an *a priori* choice of depth range over which to estimate L_{Th}. Instead, we first reordered the entire profile of σ_{600} and then identified "patches" of turbulence through the water column. Patches were identified by integrating the Thorpe displacements from the top to the bottom of the profile, and then defining patch boundaries as locations of negligible integrated displacement (see Fig. 6). Individual patches were then analyzed for patch-averaged L_{Th}, N, ε, and K_z. The value of N was based on the reordered profile of σ_{600}. For a specific depth range, such as the transition from density outflow to ambient intermediate water, we calculated depth-averaged mixing parameters from the contribution from individual patches within that range, weighted by their vertical scale.

Only mixing patches with patch height $L_P > 7dz$ (= 1.75 m) were treated as real (Galbraith and Kelley, 1996). The noise

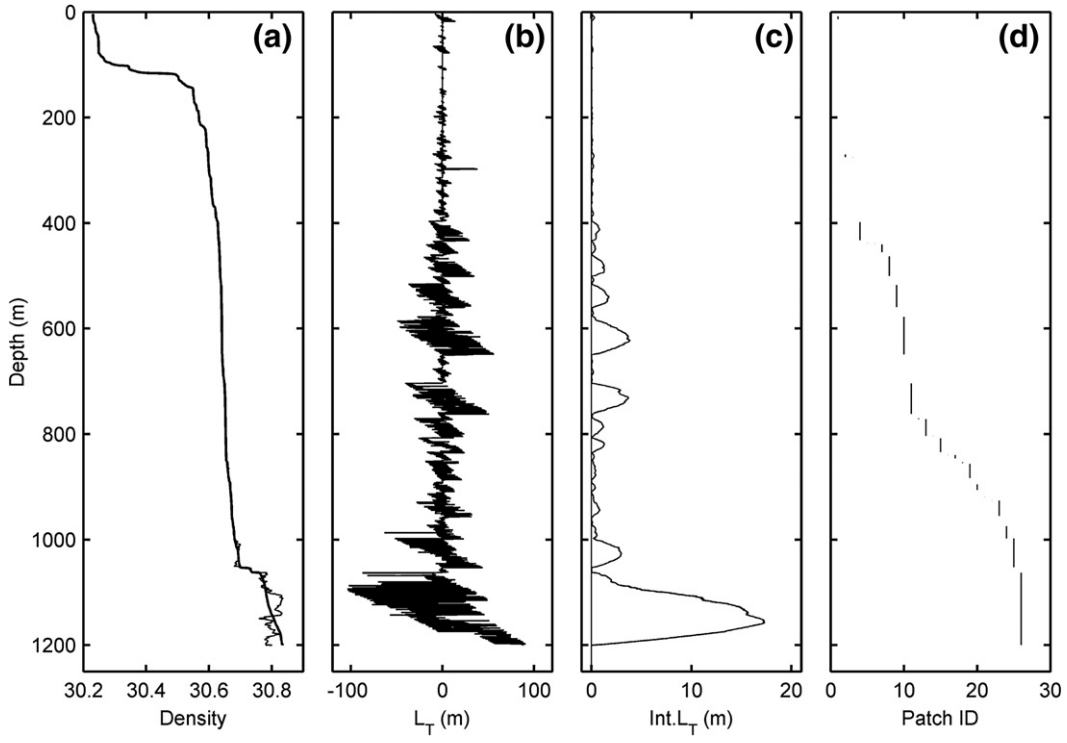

Fig. 6. Example of Thorpe reordering to identify patches, applied to CTD 37 (Group Ca). (a) Profile of measured potential density referenced to 600 hPa (σ_{600}) before (thin line) and after (thick line) reordering to a statically stable profile. (b) Thorpe displacement L_T, the vertical distance that each water "parcel" must be moved to achieve static stability. (c) Integrated Thorpe displacement (Int.L_T), beginning integration from zero at the surface. (d) Patch numbers identified from Int. L_T: patch boundaries are taken as points where Int.L_T drops below a threshold of 0.25 m, then vertical averaging scale for σ_{600} for this data set. Averaged properties are calculated per patch, and assigned throughout the depth range occupied by the patch.

level in σ_{600} was estimated as 1.5×10^{-4} kg m^{-3}, the rms value of potential density fluctuations derived from quiet segments of σ_{600} profiles. Weighted averages of mixing parameters were computed for each layer at each station as described above, and these averages were used to estimate a mean Thorpe-based diapycnal diffusivity (K_z^{Th}) for each group (Table 2).

Our second approach to estimating mixing in the transition region is based on the novel set of data obtained during AnSlope I with the CMiPS profiler (see Section 2.3). For reasons described in Section 2.3, we are unsure of the quality of the scalar microstructure data obtained with CMiPS during this cruise. Nevertheless, we present the analyses of CMiPS data to compare with the more routine Thorpe analysis approach described above.

Diffusivity was estimated from CMiPS using the method described in Osborn and Cox (1972):

$$K_z^{O-C} = \frac{3\sigma^2(\theta_z)}{(\overline{\theta}_z)^2}\kappa_T. \quad (2)$$

In Eq. (2), $\sigma^2(\theta_z)$ is the estimated variance of microstructure temperature gradient (see below), κ_T is the molecular diffusivity of heat ($\sim1.4\times10^{-7}$ m^2 s^{-1} at cold temperatures) and $\overline{\theta}_z$ is the mean temperature gradient. The FP-07 thermistors on CMiPS cannot resolve the complete spectrum of θ_z for energetic turbulence because of their relatively slow response time and the rapid descent rate of the CTD, $w_{CTD}\approx0.8$ m s^{-1}. In an attempt to compensate for this, we first calculated the measured spectrum of θ_z (attenuated at high wave numbers) over patches identified by Thorpe reordering (see above). For each patch, we then corrected the spectrum at higher wave numbers using the estimated transfer function for the FP-07 thermistors (Gregg, 1999), then fit the "universal" Batchelor spectrum to the corrected spectrum (Dillon and Caldwell, 1980). The integral of the best-fit Batchelor spectrum was then used for $\sigma^2(\theta_z)$ in Eq. (2).

Fig. 12 in Gregg (1999) shows that the efficacy of this approach, especially for the high fall speeds used here ($w_{CTD}\approx0.8$ m s^{-1}) and the hypothesized energetic mixing at the outflow's upper interface, is sensitive to the accuracy of the spectral corrections at high wave numbers. For example, if $\varepsilon=10^{-7}$ m^2 s^{-3}, capturing 50% of $\sigma^2(\theta_z)$ requires integrating the Batchelor spectrum to ~60 cycles per meter, at which wave number the approximate spectral correction is of order 10.

With these significant instrumental limitations in mind, we nevertheless attempted to estimate values of K_z^{O-C} for defined interfaces, for comparison with K_z^{Th}. We followed a similar procedure as we used for averaging Thorpe-derived mixing parameters to a specific depth interval; weighting the contribution of each patch-averaged quantity within the depth range by the fraction of the depth range occupied by the patch.

Group-averaged values of diffusivity estimated from both Thorpe reordering and CMiPS analyses (Table 2) imply mixing in the outflow's upper interface that is always energetic ($K_z>10^{-3}$ m^2 s^{-1}), with a maximum value of $\sim5\times10^{-2}$ m^2 s^{-1}. While there are several potential sources of significant error in estimating K_z from each method used here, the general agreement between the derived values from both techniques improves our confidence that the mixing estimates represent the true conditions in the transition region at the top of the density outflow.

Table 3
Mixing rates evaluated at the entrainment interface for two summer 2003 profiles (CTD-37 and CTD-179) having fairly well-mixed outflows separated by well-defined interfaces.

	CTD-37	CTD-179
$\Delta\rho_i$ (kg m^{-3})	0.11	0.24
ΔU_i (m s^{-1})	0.75	0.45
H_b	208	260
Fr	1.6	0.58
H_i (m)	58	45
Ri	0.11	0.65
K_z^{Th} (m^2 s^{-1})	0.049	0.011
K_z^{O-C} (m^2 s^{-1})	0.024	0.015
Pr	1.5	4.2
$A_z^{Th}=Pr\,K_z^{Th}$ (m^2 s^{-1})	0.075	0.047
$A_z^{O-C}=Pr\,K_z^{O-C}$ (m^2 s^{-1})	0.036	0.064
$\lvert\tau_i\rvert$ (Pa)	0.65	0.63
w_e (mm s^{-1}, m day^{-1}) from A_z^{Th}	1.29, 112	1.04, 90
w_e (mm s^{-1}, m day^{-1}) from A_z^{O-C}	0.86, 75	1.4, 120

Shown are: density and velocity steps ($\Delta\rho_i$ and ΔU_i) at the interface of thickness H_i; interfacial Richardson number, Ri (Eq. (3)); scalar eddy diffusivity K_z^{O-C} (Eq. (2)); K_z^{Th} based on Thorpe reordering of density; turbulent Prandtl number, Pr (Eq. (4)); eddy viscosity, A_z^{Th} and A_z^{O-C} based on K_z^{Th} and K_z^{O-C}, respectively; magnitude of the interfacial turbulent stress, $|\tau_i|$; and the entrainment rate, w_e, from Eq. (5).

We estimated entrainment rate w_e using both K_z^{O-C} and K_z^{Th} for two profiles (stations 37 and 179) from the upper slope. These profiles are not typical of other outflow profiles observed in summer 2003: their interfaces are sharp, and the dense water source is fHSSW rather than sHSSW. The analysis procedure for these relatively thin transition layers is, however, well developed (see, e.g., Baringer and Price, 1997). The relevant benthic layer characteristics are presented in Table 3. First we estimated turbulent vertical viscosity A_z via the Prandtl number, $Pr=A_z/K_z$, where Pr is expected to be a function of the gradient Richardson number,

$$Ri = \frac{g}{\rho_0}\frac{\Delta\rho H_i}{(\Delta U)^2}. \quad (3)$$

In Eq. (3), H_i is the interface thickness and ΔU is the magnitude of the velocity difference across the interface. Since the LADCP velocity profile is attenuated at short wavelengths, we equated ΔU with δu, i.e., we assume that velocity is constant with depth above and below the interface so that all shear was across the same depth range occupied by the region of strong hydrographic gradients. We obtained $Pr=f(Ri)$ from Blanke and Delecluse (1993), following Pacanowski and Philander (1981):

$$Pr = A_z/K_z = 1/\left(\kappa_T + (1+aRi)^{-1}\right), \quad (4)$$

where a is a constant ($=5$). These values are 1.5 and 4.2 for CTD 37 ($Ri=0.11$) and CTD 179 ($Ri=0.65$), respectively. Rohr et al. (1988) summarize estimates of $Pr(Ri)$ from multiple sets of measurements, with their best-fit curve (their Fig. 6) suggesting $Pr\approx0.7$ and 2.0 for CTDs 37 and 179. Given the significant scatter of observations of Pr in Rohr et al. (1988) and the difficulty of measuring the velocity shear used to

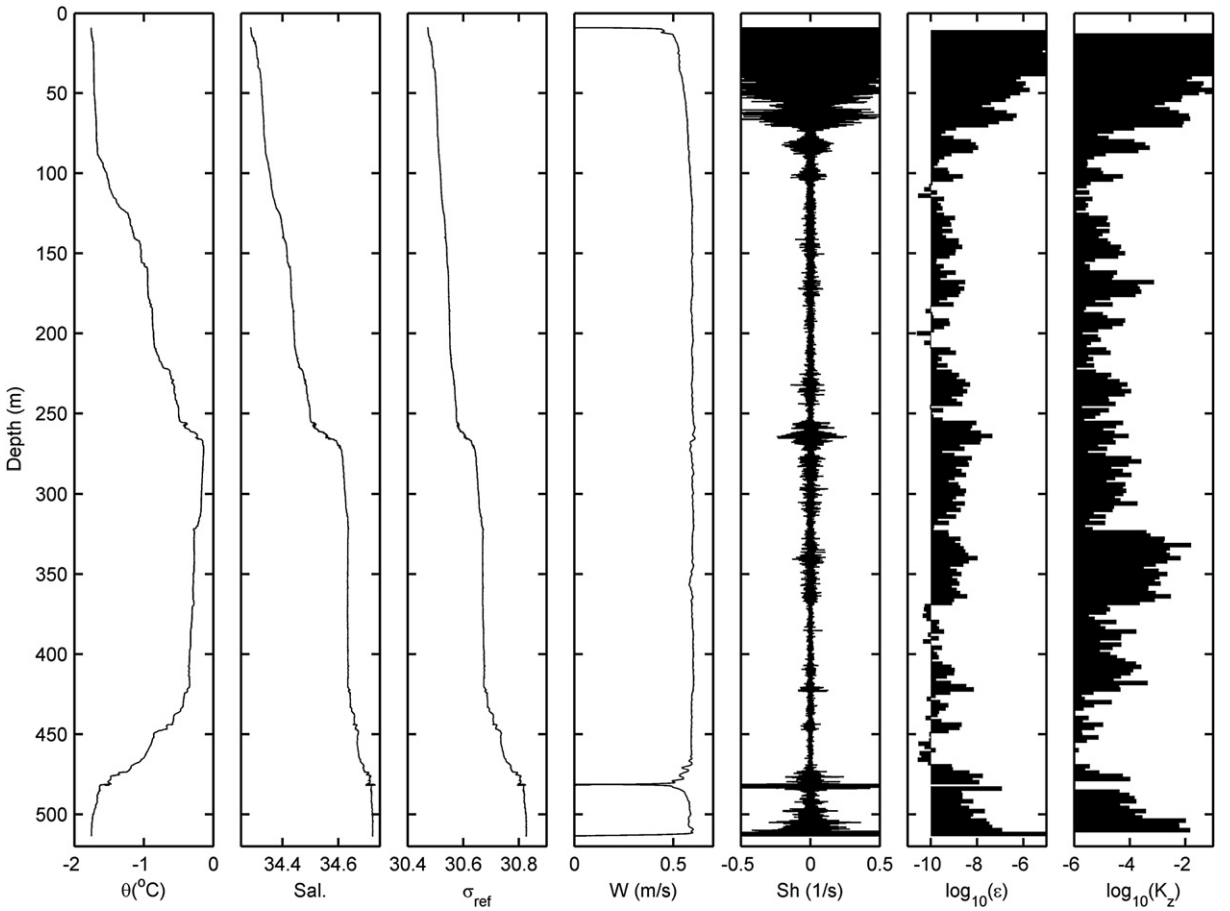

Fig. 7. Profiles from VMP-038, the last VMP profile in the time series of microstructure sampling over the Drygalski Trough sill in austral winter 2004. See Fig. 2 for profile location. From left to right: potential temperature, θ; salinity, S; potential density referenced to 600 hPa, σ_{600}; fall speed, W (m s^{-1}); microscale shear (Sh), low-passed at 35 Hz (s^{-1}), dissipation rate ε (m^2 s^{-3}); and diapycnal scalar diffusivity K_z (m^2 s^{-1}) assuming mixing efficiency $\Gamma = 0.2$. The drop in W and spike in shear Sh near 480 m depth reflect a precautionary cessation in descent to avoid impacting the seafloor with the tethered, but free-falling VMP.

estimate Ri, we decline a more detailed analysis of errors in Pr but assume that it is only known to a factor of ~2.

Two estimates of eddy viscosity, A_z^{O-C} and A_z^{Th}, were obtained for each interface, corresponding to eddy diffusivities $K_z{}^{O-C}$ and $K_z{}^{Th}$, respectively. We then estimated w_e by equating the interfacial stress magnitude $\tau_i = \rho_0 A_z |\partial U/\partial z|$ to the "entrainment stress" $\tau_e = \rho_0 \delta u w_e$ (Baringer and Price, 1997); i.e.,

$$w_e = A_z / H_i. \quad (5)$$

For stations 37 and 179, this method yielded values of $w_e \approx 1 \times 10^{-3}$ m s^{-1} (~100 m day^{-1}); see Table 3 for further details. This estimate of w_e is roughly 1/4–1/2 of those derived using downstream variability of hydrographic properties. As noted above, however, these two stations are not typical of the summer 2003 profiles within the outflow, nor are the mixing data of sufficiently high quality to justify further analysis of the "discrepancy". We conclude, however, that the data are generally consistent with our hypothesis that the interfacial stress associated with diapycnal mixing (and associated entrainment) at the upper edge of the outflow in summer 2003 is a significant factor in the momentum balance and downstream evolution of the hydrographic characteristics of the outflow.

3.3. Mixing in winter 2004

In winter 2004, when we did not detect the dense outflow on the continental slope north of the Drygalski Trough sill, we obtained a 26-hour (~one diurnal tidal cycle) time series of ~hourly microstructure profiles using the VMP on the outer shelf near the sill (see Fig. 2 for profiling sites). Profiles were only made to ~20 m above the seabed after the VMP crash guard proved insufficient to prevent sensor damage on the rough bottom. Wind speed during this period was ~5 m s^{-1}, and the mean drift of the ship ("parked" against an ice floe within the ice pack) relative to the underlying ocean was negligible. A typical VMP profile is shown in Fig. 7, and the turbulence characteristics for the ensemble of profiles are shown in Fig. 8.

Logistical constraints determined the time period available for this sampling: measurements were made near the start of neap tide with a typical barotropic tidal current speed of $|u|_{tide} \approx 0.2$ m s^{-1} (Fig. 9). At the previous spring tide, which peaked ~6 days prior to the VMP sampling, the

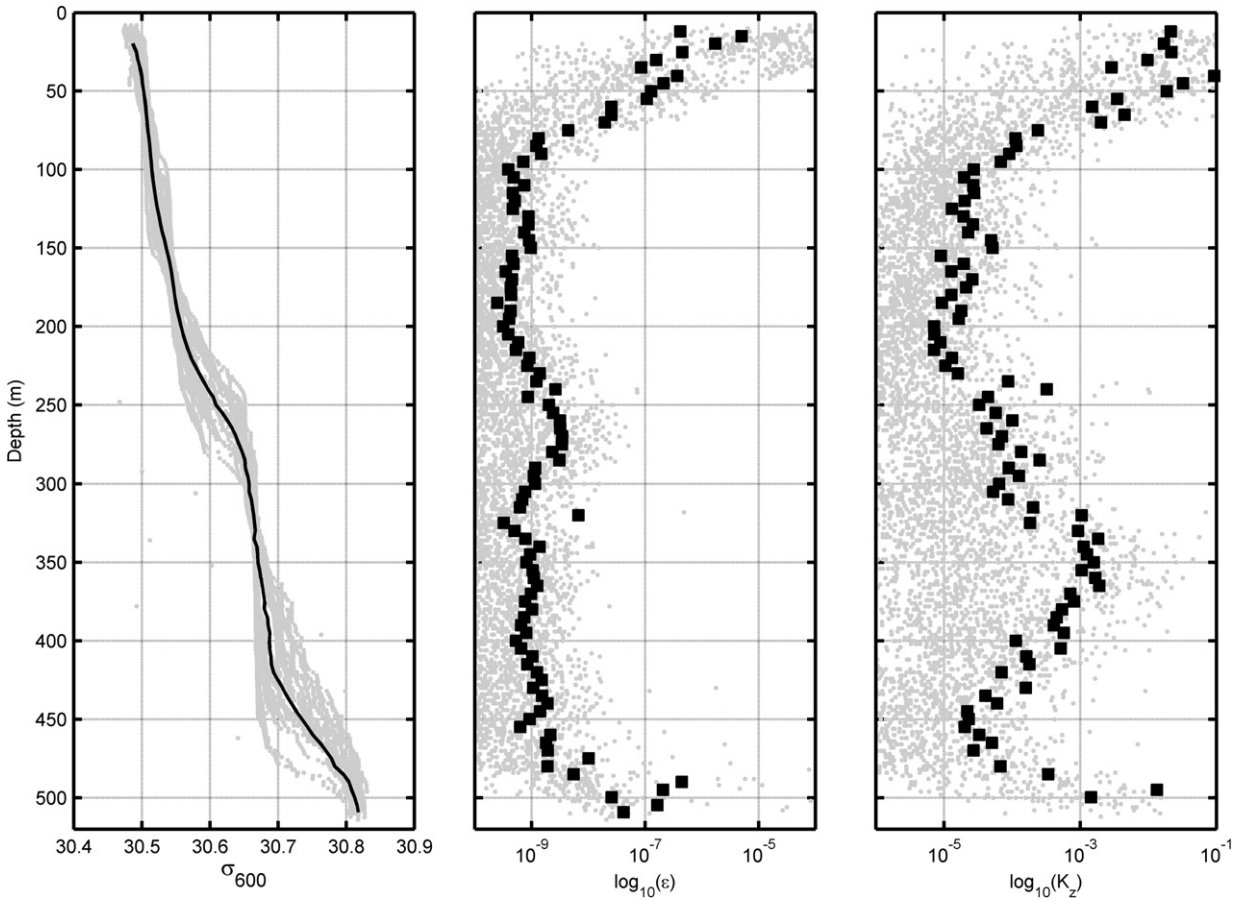

Fig. 8. Left to right: potential density referenced to 600 hPa, σ_{600}; dissipation rate ε ($m^2\ s^{-3}$); and diapycnal scalar diffusivity K_z ($m^2\ s^{-1}$), assuming mixing efficiency $\Gamma = 0.2$. Gray points show individual 2-m averaged values for each of 26 VMP profiles taken roughly hourly over the northern end of the Drygalski Trough sill (see Fig. 2 for locations). Black line (left panel) and black squares (middle and right panels) show ensemble-averaged values (an average of all 26 profiles) in 5-m depth ranges.

modeled barotropic tidal current was ~0.9 m s^{-1}. The 150 kHz VMADCP could not obtain good velocity records below ~300 m due to a lack of suitable acoustic scatterers; therefore, we do not know whether the benthic current at the time of VMP profiling was significantly different from the mostly tidal, VMADCP-measured currents higher in the water column.

We used the variance of microscale shear (from the VMP's airfoil shear probes) to calculate ε following fairly standard techniques; see, e.g., Osborn (1980) and Gregg (1987). Wave number spectra were evaluated over ~2 m blocks and corrected for attenuation at high wave numbers following Macoun and Lueck (2004). We then removed all measured shear that was coherent with the three-axis accelerometers, following a procedure developed by Lou Goodman (R. Lueck, pers. comm., 2007). Even after this noise reduction, there is a maximum wave number, which varies from block to block, above which the shear spectra no longer look like expectations for true oceanic turbulence and is assumed to be associated with vibrational modes of the tethered instrument. We identified this wave number, and estimated total shear variance, by applying an iterative technique to evaluate the wave number band over which to integrate the shear spectrum. This task is accomplished by evaluating the ratio of the measured spectrum to the fully resolved "Panchev" spectrum (Panchev and Keisch, 1969) fit to the spectral levels within a wave number band, initially 1–10 cpm. The upper wave number is then increased until a point is reached at which the extrapolated spectrum exceeds the Panchev value because of high frequency noise in the shear signal. We chose the integral of the extrapolated Panchev spectrum at this point of divergence to be the shear variance $\sigma^2(u_z)$ used for calculating ε from the standard formula (Osborn, 1980) assuming isotropy:

$$\varepsilon = \frac{15}{2}\nu\sigma^2(u_z), \tag{6}$$

where ν is the kinematic viscosity of seawater (~1.8×10^{-6} $m^2\ s^{-1}$). The diapycnal diffusivity, K_z, was then estimated from ε, following Osborn (1980):

$$K_z = \Gamma\varepsilon / \langle N^2\rangle, \tag{7}$$

where Γ is the mixing efficiency and $\langle N^2\rangle$ is the mean buoyancy frequency squared from the Thorpe-reordered profile of σ_{600} from the CTD, evaluated over the same depth interval as ε. We used $\Gamma = 0.2$ for values of K_z reported herein.

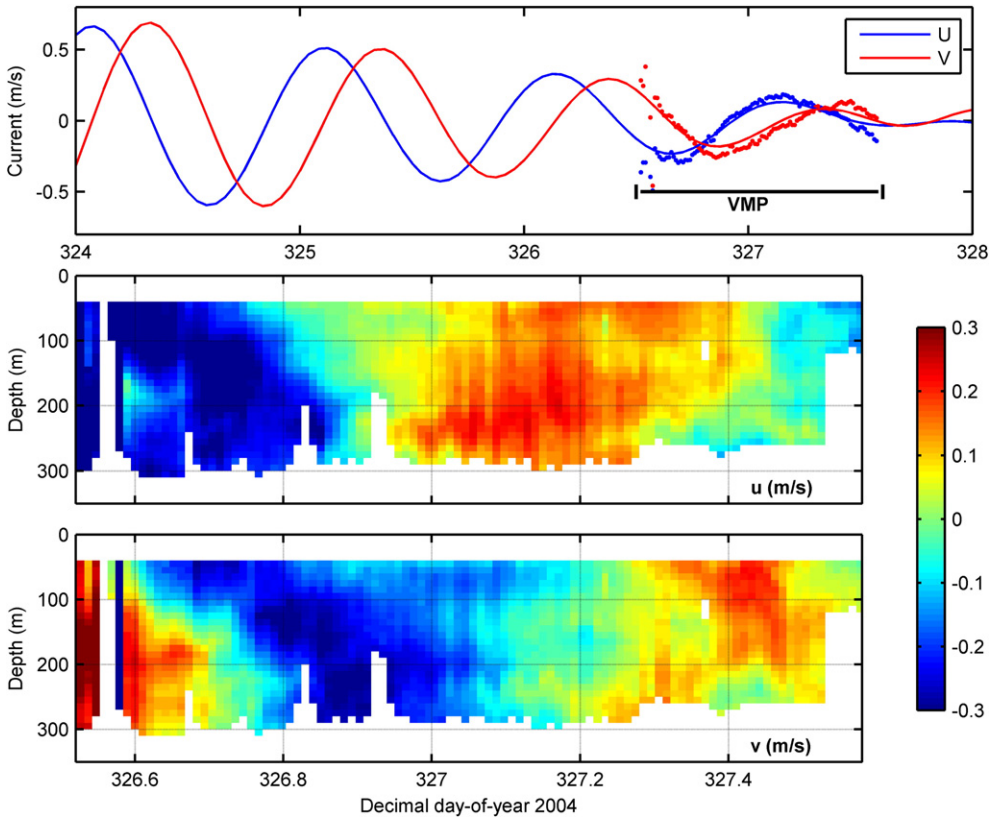

Fig. 9. Velocity fields corresponding to the VMP time series over the Drygalski Trough sill during the AnSlope 3 cruise in November 2004. (Top panel) Depth-averaged east (u) and north (v) components of current from barotropic tide model described by Erofeeva et al. (2005) (solid lines), and measured over the effective depth range ~50–300 m of the 150 kHz narrow-band, vessel-mounted ADCP (VMADCP) (dots). Modeled current is shown for the mean position of the VMP profiles. Time interval of VMP profiling is indicated. (Bottom two panels) East (u) and north (v) components of velocity from the VMADCP for the time interval of VMP profiling. Water depth of ~530 m did not vary significantly during the VMP sampling interval.

The benthic layer during VMP profiling was fHSSW, the relatively fresh type of dense shelf water (see Fig. 5d), with $\theta_b \approx T_f(P=0)$ and $S_b \approx 34.73$. The layer was actively mixing, with $\varepsilon \sim 10^{-8}$ m^2 s^{-3} and $K_z \sim 10^{-3}$–10^{-2} m^2 s^{-1} (Figs. 7 and 8). The intense upper ocean microscale shear above ~70 m depth (fifth panel from left in Fig. 7) is not consistent with the weak surface forcing at that time. We speculate, absent other obvious energy sources, that this microscale shear reflects the impact of intensive vessel thruster activity used to maintain ship position relative to the sea ice. Such thruster-generated mixing is also seen in profiles of acoustic backscatter, and may penetrate quite deeply when the upper ocean is very weakly stratified. Significant mixing was generally present throughout much of the deeper water column, with enhanced mid-depth mixing associated with the weak stratification in the core of the intrusion of relatively warm Lower Circumpolar Deep Water (LCDW) between 250 and 450 m.

The variability of σ_{600} between different profiles (Fig. 8a) suggests internal waves with vertical displacement amplitudes of order 20 m; however, the vessel drifted ~10 km during this profiling (see Fig. 2) and some of the isopycnal depth variability may be associated with spatial variability of mesoscale hydrographic structure. In every depth range, ε and K_z varied over orders of magnitude between profiles (Fig. 8b,c). Nevertheless, an ensemble average of all profiles reveals a clear vertical structure in each variable. We ignore the near-surface layer above ~100 m because we can offer only informed speculation concerning an energy source for upper ocean turbulence (see above). The high values of K_z in the intermediate layer between ~300 and ~400 m coincide with weak stratification in the core of LCDW (see Fig. 7 for typical profiles of θ and S). Some mid-depth shear is apparent in the VMADCP time series (lower panels of Fig. 9). Elevated K_z in the bottom layer is consistent with mixing by benthic stress.

No concurrent velocity data were obtained below the ~300 m range of the 150 kHz VMADCP (Fig. 9). The nearest mooring at this time was M3 (see Fig. 2 for location), near the shelf break in 791 m of water about 25 km to the north-northwest of VMP profiling. Currents at M3 during this period were fairly constant with depth from the uppermost current meter ~400 m above bottom (mab) to the lowermost current meter near 20 mab, with a typical speed of 0.4 m s^{-1}. Six days earlier, near spring tides, maximum current speeds at M3 were ~1.5 m s^{-1}. From the currents observed with the VMADCP above 300 m and the contemporaneous measurements at M3, we hypothesize that benthic flow during microstructure sampling was mostly associated with barotropic tides with a magnitude of ~0.2 m s^{-1}. We note, however, that the coldest temperature recorded at M3 during this period was ~ −0.2 °C at

10 mab, which is significantly warmer than the benthic layer sampled with microstructure (Fig. 7). This indicates the presence of a significant lateral gradient in benthic-layer hydrographic properties between the sill and shelf break. Thus, it is possible that non-tidal benthic currents may be quite different at the VMP profiling site than at M3 during this period.

3.4. Benthic stress: the impact of tides

The addition of tides modulates benthic currents at the time scale of the fundamental (predominantly diurnal) tide and also at the fortnightly spring/neap cycle caused by the superposition of the most energetic tidal harmonics, O_1 and K_1. Tidal currents in the study area range from almost negligible at neap tide to a maximum at spring tide. We expect that this variability will be reflected in the time-dependent benthic stress acting on the dense outflow, and in the associated mixing rates. The maximum tidal current exceeds 0.8 m s^{-1} along the shelf break north of the Drygalski Trough (Fig. 10), compared with ~0.4–0.6 m s^{-1} for the mean speed of the dense outflow (Gordon et al., 2004, 2008).

The only AnSlope measurements suitable for determining the mixing rates in the benthic layer were those obtained with the VMP over the sill during the winter 2004 cruise (see Section 3.3). For reasons explained above, we believe that the current near the seabed at this time was dominated by the barotropic tide, but the mean current speed was ~0.2 m s^{-1}, close to the neap tide value. The Ekman depth $D_E = \pi(2A_z/|f|)^{1/2}$ associated with these currents, assuming $K_z = 10^{-3}$–10^{-2} m^2 s^{-1} (Fig. 8c) is ~12–35 m, generally consistent with the observed benthic layer thickness at that time.

The benthic layer over the outer shelf is known to extend a few hundred meters above the seabed during spring tides (Whitworth and Orsi, 2006). We expect D_E ($\propto|\tau_b|$, i.e., $\propto|u|^2$) to increase by a factor of ~10–20 at spring tides when $|u| \approx 0.8$ m s^{-1}. The Ekman depth scale may be different from the observed bottom boundary layer thickness since the benthic stress conditions vary quite rapidly (on tidal time scales) and lateral advection of hydrographic gradients is significant at times of strong mixing.

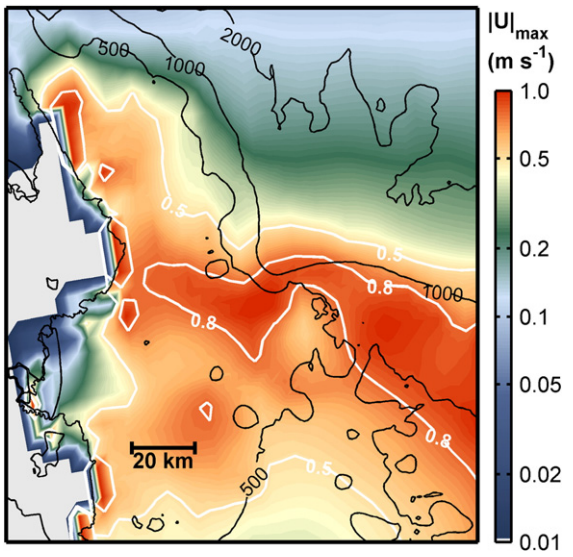

Fig. 10. Maximum tidal current speed ($|U|_{max}$) from Ross Sea barotropic tide inverse model (Erofeeva et al., 2005). Color scale (m s^{-1}) on right is logarithmic. The white contours show $|U|_{max} = 0.5$ and 0.8 m s^{-1}. Black contours show isobaths. Geographical location is indicated by the magenta rectangle on Fig. 1. A map of $|U|_{max}$ for the complete domain shown in Fig. 1 is presented by Padman et al. (2008).

Benthic hydrographic properties over the central and upper slope provide further support for the hypothesis that tides have a significant impact on outflow properties. The time series of θ_b at mid-slope mooring CD1 (Fig. 11) shows tidal variability at both daily and spring/neap time scales, including intermittent cold pulses with near-freezing θ_b; cf. Gordon et al. (2004). The warmest values of θ_b, after low-passing the signal at (1/7) cycles per day (cpd) to highlight the spring/neap variability, occur ~2–3 days after spring tide. This observation is consistent with the hypothesis that the benthic layer is significantly diluted through entrainment of the overlying warmer (and fresher) MCDW when the benthic stress is greatest during spring tides. An energy-preserving spectrum of θ_b at outer-shelf mooring CB2 (Fig. 12) shows similar dependence on tides; peaks occur at the fundamental tidal frequencies near one and two cpd, with significant energy also at the spring/neap frequency of ~(1/14) cpd.

It is difficult, however, to separate the effects of advection and mixing on benthic layer properties at specific locations. As Whitworth and Orsi (2006) and Padman et al. (2008) have shown, spring tides can carry water parcels tens of kilometers in one tidal cycle, even if the net Lagrangian drift associated with tidal rectification is ignored. Sample Lagrangian paths at spring tide (Fig. 13) show that parcels can be carried by tides from the outer shelf to mid-slope (~1500 m isobath) in 12 h.

3.5. Modeled tide-induced mixing

Given the difficulty of interpreting measurements from either the regional CTD/LADCP surveys or individual moorings, we used a three-dimensional, primitive equation ocean tide model to provide further context for our hypothesis that tides contribute to mixing of the outflow. The model is based on the Regional Ocean Modeling System version 2.2 (ROMS2.2) and uses a 1 km lateral spacing of grid nodes and 41 vertical levels in terrain-following vertical coordinates. Layer spacing decreases towards the sea surface and the seabed. Initial hydrography was obtained from the new grid described by Orsi and Wiederwohl (2008). The model was first run without forcing to develop dynamically consistent velocity and hydrographic fields. We then applied tidal forcing at all open-ocean boundaries, using barotropic tidal elevation and velocities from Erofeeva et al. (2005). Tides were forced at a single (K_1) frequency, using different scaling of the forcing amplitude to represent the approximate range of total tidal kinetic energy from neap ($0.2 \times K_1$) to spring ($2.0 \times K_1$) tides.

Vertical mixing in the model was parameterized by the Mellor-Yamada level 2.5 turbulence closure scheme (Mellor and Yamada, 1982). Benthic stress was modeled as quadratic drag with coefficient $c_d = 0.003$. Further model details are provided by Padman et al. (2008).

Fig. 14 in Padman et al. (2008) shows time series of near-seabed currents and S_b, and plots of $S(t,z)$ and $K_z(t,z)$ for sites over the outer shelf and upper slope near the Drygalski

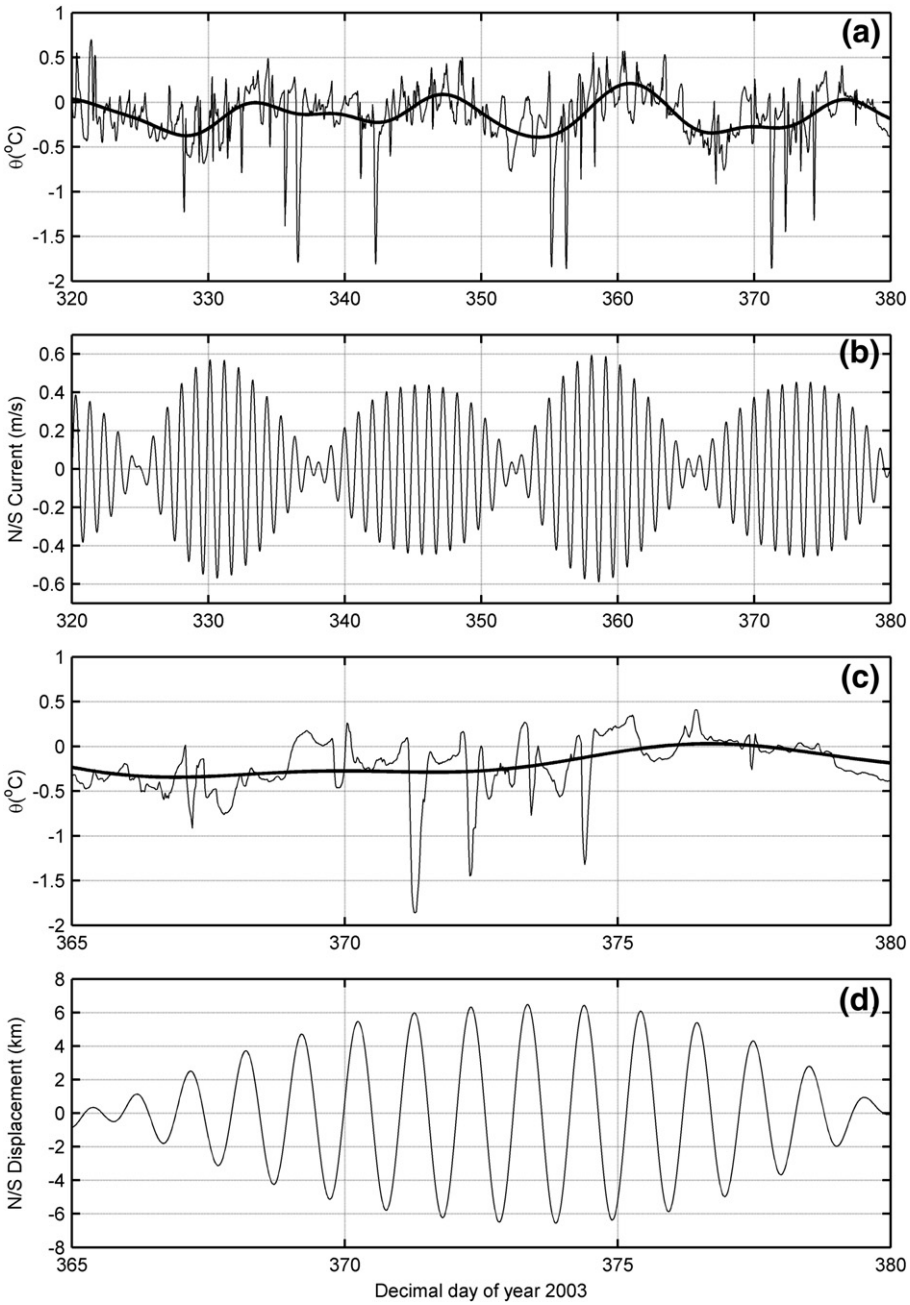

Fig. 11. (a) Potential temperature at 10 m above the seabed (θ_b) at mooring CD1 on the mid-slope (see Fig. 2 for location). Fine line is θ_b measured every 30 min; bold line is θ_b after low-pass filtering with a cutoff period of 7 days to highlight spring-neap variability. (b) *v*-component (roughly cross-slope) of modeled barotropic tidal current (m s^{-1}) at CD1. (c) Same as (a), but for days 365–380 (first two weeks of 2004). (d) Cross-slope displacement (km) by tides, based on time-integration of modeled *v* at CD1.

Trough sill during spring tide represented by $2.0\times K_1$ tidal forcing. The modeled thickness of the nearly homogeneous benthic boundary layer (BBL) varies from ~10 m to ~200 m at each site during one diurnal tidal cycle. Energetic mixing extends hundreds of meters above the BBL, however, due to shear from baroclinicity acting on the weak stratification typical of the mid-water column in this region (see Figs. 5, 7 and 8). Maximum modeled K_z over the outer shelf in the nearly homogeneous BBL was ~1 m^2 s^{-1} at spring tides. Significantly elevated values ($K_z > 10^{-4}$ m^2 s^{-1}) extended to ~400 m above the seabed, i.e., ~100 m below the sea surface.

Fig. 14 in the present paper shows the variability of $K_z(t,z)$ for two sites: Point#1 over the outer shelf and Point#2 on the upper slope, for model runs with forcing of $0.2\times K_1$ (neap tide, comparable to conditions during VMP profiling) and $2.0\times K_1$ (spring tide). Site locations are indicated on Fig. 2. The differences in mean hydrographic structure between modeled neap and spring tides are caused by the combination of

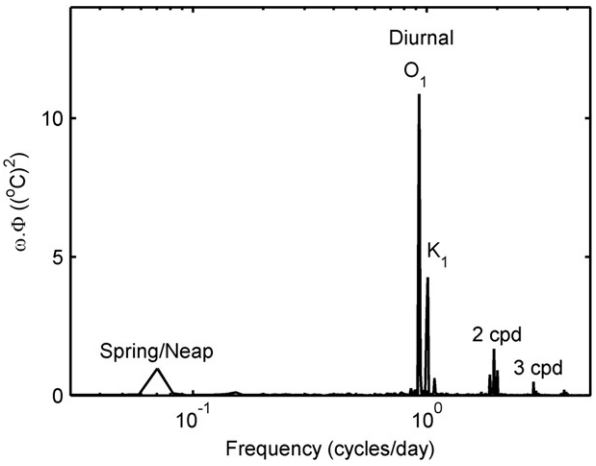

Fig. 12. Area-preserving frequency spectrum $\omega.\Phi$, where ω is the frequency and Φ is the power spectral density of potential temperature θ at ~10 m above the seabed from mooring CB2 (2004/05) on the outer continental shelf near the Drygalski Trough sill. See Fig. 2 for mooring location.

different tidal advection and the dramatically different mixing environments between the two cases. The wide range of instantaneous σ_{600} and K_z (gray dots), during the two K_1 tidal cycles (2 days) plotted, highlights the difficulty of measuring these variables during a ship-based CTD survey.

There are significant differences between the modeled profiles of K_z for neap tides over the outer shelf (Fig. 14b) and the measurements from the VMP during the winter 2004 cruise (Figs. 7 and 8). In particular, the MY2.5 turbulence closure scheme in the model produces no mid-depth mixing above the model's minimum value of $K_z = 10^{-6}$ m^2 s^{-1}. This may be explained by the difference in buoyancy frequency N in the weakly stratified mid-depth layer between the model hydrography and the VMP data. Recall that the VMP data were collected during a period in which no dense outflow was seen over the continental slope, whereas the model produces an outflow even with tidal forcing set to zero (Padman et al., 2008) because of the choice of initial hydrography. The model also produces less variability in isopycnal depth than in the VMP profiles. As previously noted, this measured variability may be associated primarily with spatial changes as the ship drifted with the ice; however, it may also indicate internal wave generation that has not been adequately represented in the model.

Although the measured mid-depth mixing is not represented by the model, the mean thickness of the benthic layer and the mean values of K_z in each case are similar, as are the spreads of values through the tidal cycle. This gives us some confidence that the much higher, and more extremely varying, values of modeled K_z in and above the BBL during spring tides (Fig. 14d) are at least qualitatively consistent with real ocean mixing over the outer shelf at those times. That is, as suggested by Whitworth and Orsi (2006), energetic mixing

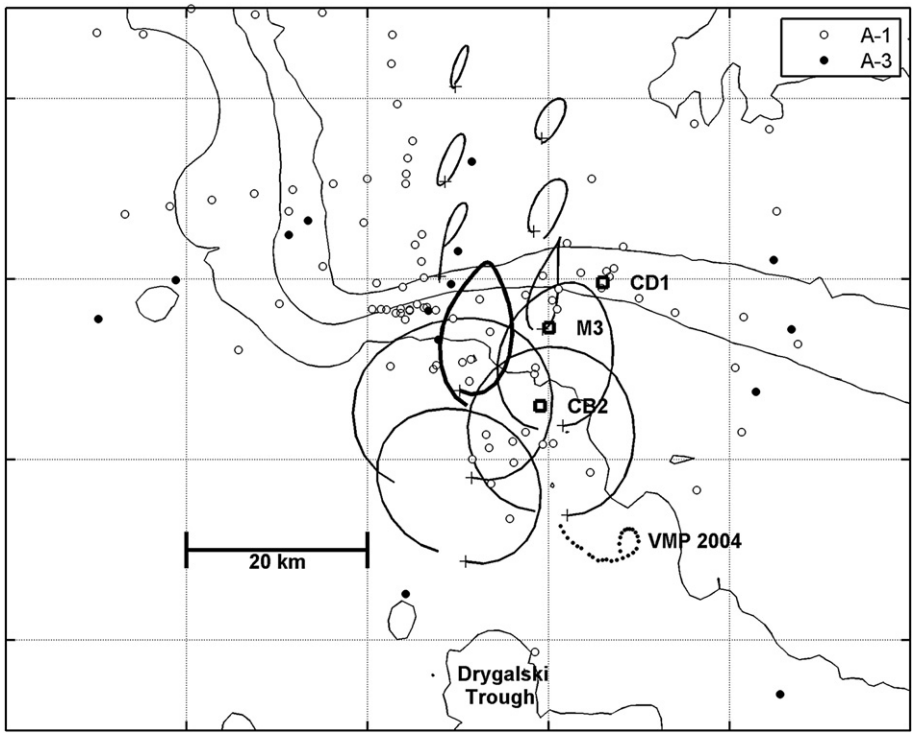

Fig. 13. Sample Lagrangian drifter trajectories near the Drygalski Trough sill for 25 h during spring tides, from a barotropic tide-only model. The release location for each drifter (+), CTD stations for AnSlope 1 (open circles) and AnSlope 3 (filled circles) are shown. Moorings referred to in the text are indicated. Contours show the 530, 1000, 1500 and 2000 m isobaths. The bold drifter trajectory extends from several km inshore of the shelf break to near the 1500 m isobath. Ellipses are not closed because of tidal rectification and because the tide is comprised of the superposition of several harmonics having distinct frequencies.

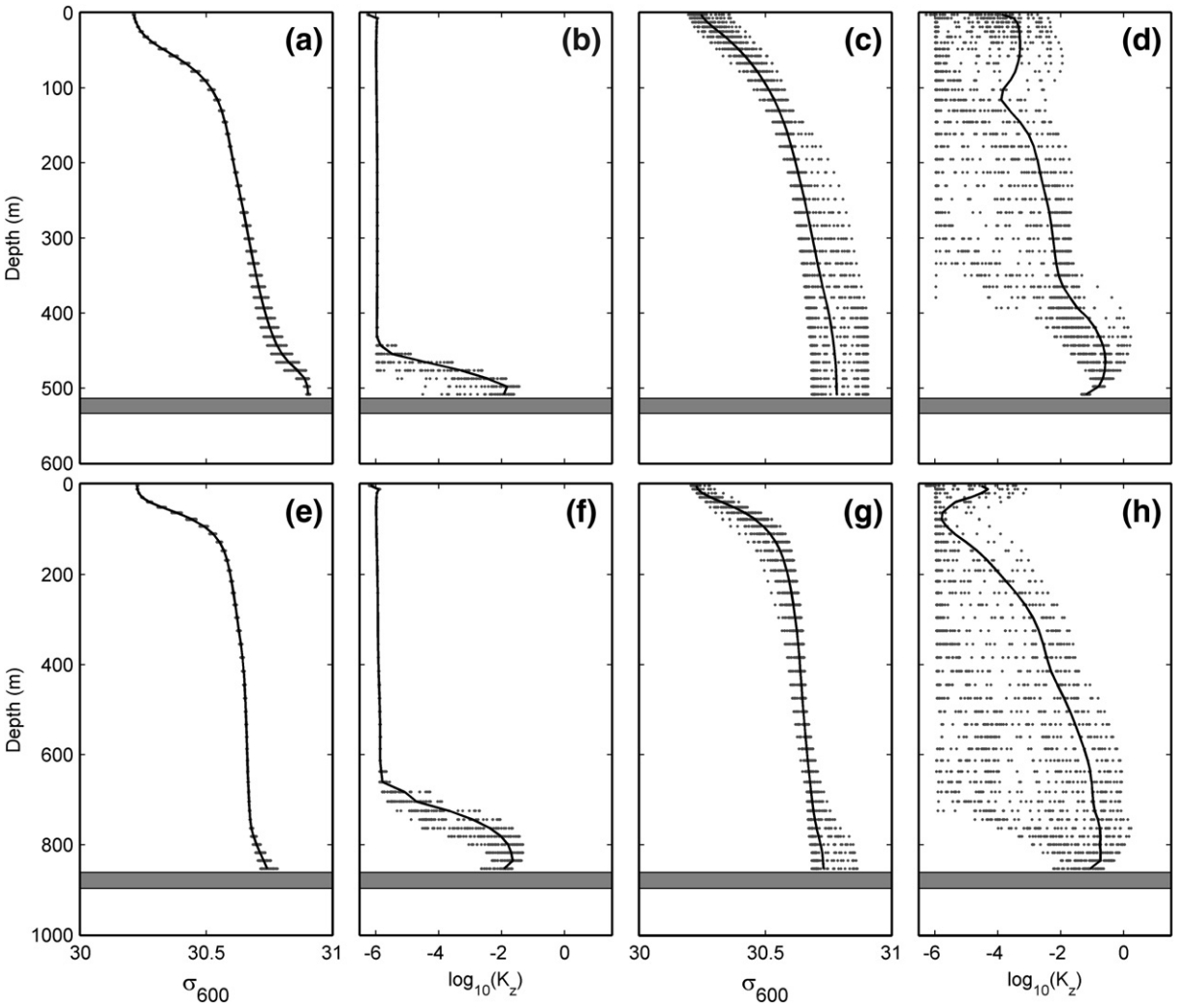

Fig. 14. Modeled potential density referenced to 600 hPa (σ_{600}) and vertical diffusivity K_z ($m^2\ s^{-1}$) for Point#1 on the outer continental shelf north of the Drygalski Trough sill (upper panels) and at a nearby site (Point#2) on the upper slope. See Fig. 2 for site locations. For each panel, the gray dots represent hourly instantaneous values at the 41 model levels, and the black line represents the average profile over two K_1 tidal cycles (2 days). Upper panels: (a) and (b) σ_{600} and $\log_{10}(K_z)$ for $0.2\times K_1$ forcing ("neap tides"); (c) and (d) σ_{600} and $\log_{10}(K_z)$ for $2.0\times K_1$ forcing ("spring tides"). Lower panels: As for upper panels, but for Point#2. The top of the thick gray boxes at the bottom of each panel shows the model water depth.

extends throughout much of the water column during spring tides. Values of K_z in the lower water column are of order 0.1–1 $m^2\ s^{-1}$, indicating rapid smoothing of the hydrographic structure over the shelf; compare the mean profiles of σ_{600} in Fig. 14a and c. The hydrographic structure is maintained, in the presence of this active mixing at spring tides, by advection; a column of water passes across the region of active tidally driven mixing in a few days if the mean flow is of order 0.1 m s^{-1} over the shelf (Jaeger et al., 1996; Padman et al., 2008).

We can compare the modeled contribution of tides to the net benthic stress through a simple model of an outflow without and with tides. We estimate bottom stress τ_b from the quadratic drag law, $\tau_b = \rho_0 c_d |u| u$, where the drag coefficient c_d is taken to be 0.0025. While uncertainties in bottom physical characteristics may justify the choice of different c_d with a commensurate effect on the magnitude of τ_b, the ratio of mean stress with and without tides is independent of this value. For simplicity, even though the fundamental tidal frequency $\omega_{tide} \sim 0.5f$, we assume that the boundary layer remains in steady-state at all times. For a typical outflow speed (no tides) of $|u| = 0.6$ m s^{-1}, the magnitude of the stress opposing the flow is $\tau_b \approx 0.9$ Pa (Table 4). The quadratic dependence of stress on $|u|$ causes the *time-averaged* stress to increase when periodic tidal currents are added (Robertson et al., 1998). Assuming a typical spring tidal current of 0.8 m s^{-1} across-slope and 0.4 m s^{-1} along-slope, the stress averaged over one tidal cycle at spring tides is $\langle \tau_b \rangle \approx 1.5$ Pa, ~60–70% greater than for the no-tides case. Assuming that $A_z \propto |\tau_b|$ (Pond and Pickard, 1986, pp. 108–109), the time-averaged value of A_z is increased by a factor of ~2 while the mean Ekman depth $D_E = \pi(2A_z/|f|)^{1/2}$ and cross-stream Ekman volume flux $Q_E = \tau_b/(\rho_0 f)$ scale directly with the increased mean along-flow stress. The maximum value for D_E during the spring tidal cycle is

Table 4
Impact of adding oscillatory spring tidal currents to the mean outflow (see text for details) on mean properties of the bottom frictional ("Ekman") boundary layer, assuming eddy viscosity $K_m(t) \propto |\tau_b(t)/\rho_o| = c_d|u(t)|^2$; $c_d = 0.0025$.

	No tides	Spring tides
$\langle K_m \rangle$ ($m^2\ s^{-1}$)	0.09	0.19
$\langle \lvert\tau_a\rvert \rangle$ (Pa)	0.9	1.4
$\langle D_E \rangle$ (m)	114	157
(range)		(38–202)
$\langle Q_E \rangle$ ($m^2\ s^{-1}$)	6.5	10.1
$\langle v_E \rangle$ ($cm\ s^{-1}$)	5.7	6.4

Mean values through one tidal cycle are denoted by angle brackets $\langle . \rangle$. Values are tabulated for time-averaged along-outflow benthic stress $\langle |\tau_a| \rangle$, Ekman depth $\langle D_E \rangle$, cross-stream Ekman volume flux $\langle Q_E \rangle$, and cross-stream velocity averaged over the Ekman layer, $\langle v_E \rangle$. The range of D_E through the tidal cycle is also shown.

~200 m, or about twice the no-tides value of 114 m. This value is comparable to the maximum BBL thickness in our three-dimensional, primitive equation model (Fig. 14 in Padman et al., 2008).

4. Conclusions

We have observed energetic mixing of a benthic outflow of dense Antarctic shelf water through measurements of temperature, salinity, currents, and microstructure over the outer shelf and slope of the northwest Ross Sea. The maximum Froude number is $Fr \approx 1.8$ over the upper slope. Downstream variability of the outflow's hydrographic properties (Gordon et al., 2004) is consistent with an entrainment rate $w_e \approx 2$–4 mm s^{-1}, or ~200–400 m day^{-1}. These values are comparable to those from other regions with $Fr > 1$. The angle of the outflow relative to isobaths (~35°; Gordon et al., 2004, 2008) is, however, significantly higher than most previously reported values, which are of order 10°. This may reflect physical processes such as the unusually strong tides of the region (Fig. 10) or the extremely steep continental slope, of order 1:6 in the vicinity of the outflow's initial descent across the shelf break.

The quality and number of microstructure profiles obtained through the outflow was limited by small horizontal scales of topographic and hydrographic variability, a large tide-induced cross-slope advection of the outflow, and logistic constraints imposed by sea ice on ship-based sampling. Nevertheless, scalar fine structure and microstructure measurements through the sharp interface atop the outflow on the upper slope imply an entrainment rate of ~1 mm s^{-1} (~100 m day^{-1}), and are consistent with our expectation that mixing associated with interfacial shear plays a significant role in downstream dilution of the outflow. This shear is largely explained by the dynamics associated with the density flow over the slope. Other potentially important processes such as baroclinic waves excited along the slope may also contribute to interfacial shear and will be addressed in future modeling studies.

Analyses of time series measurements from moored arrays (Figs. 11 and 12; Gordon et al., 2004; Whitworth and Orsi, 2006; Gordon et al., 2008), and of the time variability among closely spaced hydrographic profiles, strongly implicate tides as a critical missing factor in our dynamical understanding of this outflow. Tides in the outflow region are energetic, with peak currents at spring tide exceeding 0.8 m s^{-1} along the outer shelf and upper slope (Fig. 10; Erofeeva et al., 2005; Padman et al., 2008). Numerical models suggest that the tides are primarily barotropic (Robertson, 2005; Padman et al., 2008): if so, their contribution to interfacial shear atop the outflow will be small. Tidal currents do, however, significantly increase the time-averaged benthic stress (Fig. 14, Table 4). We estimate that the addition of spring tides increases the mean vertical eddy viscosity A_z of the benthic mixed layer by a factor of ~2, and downslope Ekman transport and Ekman mixing depth by ~60–70% relative to the case for the Drygalski Trough outflow with no tides. Based on mooring data (Whitworth and Orsi, 2006) and output from our three-dimensional, tide-forced ocean model (Padman et al., 2008), mixing driven by benthic stress at spring tides may be sufficiently vigorous to augment shear-driven entrainment at the outflow's upper interface (Fig. 14). Microstructure measurements of mixing over the outer shelf, even though obtained close to neap tide ($|u| \approx 0.2$ m s^{-1}), support our view that tidal mixing is a critical ingredient in preconditioning the dense water exiting the Drygalski Trough by mixing with overlying MCDW. When these measurements are scaled up to spring tides, the mixing would be sufficiently vigorous to mix through the lower ~200–400 m of the water column over the sill and outer shelf, as suggested by our model (Fig. 14). The model suggests a similar spring-neap cycle of mixing over the upper continental slope where maximum tidal currents are similar to those over the outer shelf.

The complex interaction among cross-slope advection by tides, tidal mixing due to benthic stress over the sill and upper slope, interfacial mixing associated with shear between the outflow and overlying ambient fluid, and the pronounced spring-neap cycle in both advection and mixing rates, all in a region where the spatial scales of the outflow are small and cross-slope bathymetry is steep, creates a significant challenge in both measuring and modeling the outflow. Further work on dense outflows from Antarctic shelves must take this complexity into account, since it is unlikely that either field programs or models can adequately represent the volume and hydrographic characteristics of the outflows without explicit identification of the role of tides.

Other processes, not yet addressed, undoubtedly contribute to the ultimate fate of dense shelf water exiting the western Ross Sea. These processes include modifications to the large-scale circulation caused by seasonal and synoptic variability of the atmospheric forcing and sea ice cover, seasonal variations in dense water production further south on the Ross Sea continental shelf, and the potential for thermobaricity to influence the fate of dense water forced downslope by cross-slope tidal currents (Foldvik et al., 2004). In addition, the outflow may couple with the dynamics of the slope current associated with the Antarctic Slope Front (see Baines, 2008 for further discussion of the ASF). While the slope current is surface-intensified, it has maximum along-slope currents of ~0.5 m s^{-1}, and the vertical shear associated with it may contribute to driving entrainment at the outflow's upper interface. Finally, small-scale bathymetric features known to be present on the slope (Davey and Jacobs, 2007) may impact the trajectory of, and mixing associated with, the outflow. These

processes are being assessed in ongoing studies utilizing further data analyses and numerical modeling.

Acknowledgements

We gratefully acknowledge the critical contribution to AnSlope provided by Captain Joe Borkowski (AnSlope 1), Captain Mike Watson (AnSlope 3), the crew of the *N. B. Palmer*, and the Raytheon Polar Services technical support team led by Karl Newyear. We thank Chris MacKay for his tireless support of CMiPS operations at sea during AnSlope 1, Loren Mueller for his assistance with VMP profiling during AnSlope 3, Bruce Huber and Phil Mele for their attention to producing a top quality CTD and LADCP data set, and Lana Erofeeva and Susan Howard for tide modeling. Constructive and helpful comments were provided by Tamay Özgökmen and an anonymous reviewer. This study was funded by the NSF Office of Polar Programs through grants OPP-0125602 and ANT-0440656 to ESR, OPP-0125172 and ANT-0440823 to LDEO, and OPP-0125084 and ANT-0440657 to TAMU, and ONR grant N00014-03-1-0067 to ESR. This is ESR contribution number 098 and LDEO contribution number 7225.

References

Baines, P., 2008. A model for the structure of the Antarctic Slope Front. Deep-Sea Res. II 55.

Baines, P.G., Condie, S., 1998. Observations and modeling of Antarctic downslope flows: A review. In: Jacobs, S.S., Weiss, R.F. (Eds.), Ocean, Ice, and Atmosphere: Interactions at the Antarctic continental margin. Antarctic Research Series, vol. 75. AGU, Washington, pp. 29–49.

Baringer, M.O., Price, J.F., 1997. Momentum and energy balance of the Mediterranean outflow. J. Phys. Oceanogr. 27, 1678–1692.

Bindoff, N.L., Rosenberg, M.A., Warner, M.J., 2000. On the circulation and water-masses over the Antarctic continental slope and rise between 80 and 150°E. Deep-Sea Res. II 47, 2299–3326.

Blanke, B., Delecluse, P., 1993. Variability of the tropical Atlantic Ocean simulated by a general circulation model with two different mixed-layer physics. J. Phys. Oceanogr. 23, 1363–1388.

Davey, F.J., Jacobs, S.S., 2007. Influence of submarine morphology on bottom water flow across the western Ross Sea continental margin, Antarctica. In: Cooper, A.K., Raymond, C.R., et al. (Eds.), A Keystone in a Changing World, Online Proceedings of the 10th ISAES. USGS Open-File Report 2007-1047. doi:10.3133/of2007-1047.srp067.

Dillon, T.M., 1982. Vertical overturns: A comparison of Thorpe and Ozmidov length scales. J. Geophys. Res. 87, 9601–9613.

Dillon, T.M., Caldwell, D.R., 1980. The Batchelor spectrum and dissipation in the upper ocean. J. Geophys. Res. 85, 1910–1916.

Erofeeva, S.Y., Egbert, G.D., Padman, L., 2005. Assimilation of ship-mounted ADCP data for barotropic tides: Application to the Ross Sea. J. Atmos. Ocean. Technol. 22 (6), 721–734.

Foldvik, A., Gammelsrød, T., Østerhus, S., Fahrbach, E., Rohardt, G., Schröder, M., Nicholls, K., Padman, L., Woodgate, R., 2004. Ice shelf water overflow and bottom water formation in the southern Weddell Sea. J. Geophys. Res. 109, C02015. doi:10.1029/ 2003JC002008.

Galbraith, P.S., Kelley, D.E., 1996. Identifying overturns in CTD profiles. J. Atmos. Ocean. Tech. 13, 688–702.

Gill, A.E., 1973. Circulation and bottom water formation in the Weddell Sea. Deep-Sea Res. 20, 111–140.

Gordon, A.L., 1998. Western Weddell Sea thermohaline stratification. In: Jacobs, S.S., Weiss, R.F. (Eds.), Ocean, Ice, and Atmosphere: Interactions at the Antarctic continental margin. . Antarctic Res. Ser., vol. 75. AGU, Washington, pp. 215–240.

Gordon, A.L., Zambianchi, E., Orsi, A., Visbeck, M., Giulivi, C.F., Whitworth III, T., Spezie, G., 2004. Energetic plumes over the western Ross Sea continental slope. Geophys. Res. Lett. 31, L21302. doi:10.1029/2004GL020785.

Gordon, A.L., Orsi, A.H., Muench, R.D., Huber, B.A., Zambianchi, E., Visbeck, M., 2008. Western Ross Sea continental slope gravity currents. Deep-Sea Res. II 55.

Gregg, M.C., 1987. Diapycnal mixing in the thermocline: A review. J. Geophys. Res. 92, 5249–5286.

Gregg, M.C., 1999. Uncertainties and limitations in measuring ε and χ_T. J. Atmos. Ocean. Technol. 16 (11), 1483–1490.

Holland, D.M., Rosales, R.R., Stefanica, D., Tabak, E.G., 2002. Internal hydraulic jumps and mixing in two-layer flows. J. Fluid Mech. 470, 63–83.

Jacobs, S.S., Amos, A.S., Bruchhausen, P.M., 1970. Ross Sea oceanography and Antarctic Bottom Water formation. Deep-Sea Res. 17, 935–962.

Jaeger, J.M., Nittrouer, C.A., DeMaster, D.J., Kelchner, C., Dunbar, R.B., 1996. Lateral transport of settling particles in the Ross Sea and implications for the fate of biogenic material. J. Geophys. Res. 101, 18,479–18,488.

Johnson, G.C., 2008. Quantifying Antactic Bottom Water and North Atlantic Deep Water volumes. J. Geophys. Res. 113, C05027. doi:10.1029/ 2007JC004477.

Killworth, P.D., 1977. Mixing on the Weddell Sea continental slope. Deep-Sea Res. 24, 427–448.

Legg, S., Chang, Y., Chassignet, E., Danabasoglu, G., Ezer, T., Gordon, A., Griffies, S., Hallberg, R., Jackson, L., Large, W., Özgökmen, T., Peters, H., Price, J., Riemenschneider, U., Wu, W., Xu, X., Yang, J., 2009. Improving oceanic overflow representation in climate models: the Gravity Entrainment Climate Process Team. Bull. Am. Meteorol. Soc. 90.

Locarnini, R.A., 1994. Water masses and circulation in the Ross Gyre and environs. Ph.D. Dissertation, Texas A&M Univ., 87 pp.

Macoun, P., Lueck, R., 2004. Modeling the spatial response of the airfoil shear probe using different sized probes. J. Atmos. Ocean. Technol. 21 (2), 284–297.

Mellor, G.L., Yamada, T., 1982. Development of a turbulence closure model for geophysical fluid problems. Rev. Geophys. Space Phys. 20 (4), 851–875.

Orsi, A.H., Wiederwohl, C.L., 2008. A recount of Ross Sea waters. Deep-Sea Res. Part II 55.

Orsi, A., Johnson, G., Bullister, J., 1999. Circulation, mixing and production of Antarctic Bottom Water. Prog. Oceanogr. 43, 55–109.

Osborn, T.R., 1980. Estimates of the local rate of vertical diffusion from dissipation measurements. J. Phys. Oceanogr. 10, 83–89.

Osborn, T.R., Cox, C.S., 1972. Oceanic fine structure. Geophys. Fluid Dyn. 3, 321–345.

Pacanowski, R.C., Philander, S.G.H., 1981. Parameterization of vertical mixing in numerical models of tropical oceans. J. Phys. Oceanogr. 11, 1443–1451.

Padman, L., Fricker, H.A., Coleman, R., Howard, S., Erofeeva, S., 2002. A new tidal model for the Antarctic ice shelves and seas. Ann. Glaciol. 34, 247–254.

Padman, L., Erofeeva, S., Joughin, I., 2003. Tides of the Ross Sea and Ross Ice Shelf cavity. Antarct. Sci. 15, 31–40.

Padman, L., Howard, S.L., Orsi, A.H., Muench, R.D., 2008. Tides of the Northwestern Ross Sea and their impact on dense outflows of Antarctic Bottom Water. Deep-Sea Res. II 55. doi:10.1016/j.dsr2.2008.10.026.

Panchev, S., Keisch, D., 1969. Energy spectrum of isotropic turbulence at large wavenumbers. Dokl. Bolg. Akad. Nauk 22, 627–630.

Peters, H., Johns, W.E., 2005. Mixing and entrainment in the Red Sea outflow plume. Part II: Turbulence characteristics. J. Phys. Oceanogr. 35, 584–600.

Polzin, K., Kunze, E., Hummon, J., Firing, E., 2002. The finescale response of lowered ADCP velocity profiles. J. Atmos. Ocean. Technol. 19, 205–224.

Pond, S., Pickard, G.L., 1986. Introductory Dynamical Oceanography, 2nd Edition. Pergamon, Oxford.

Rintoul, S., 1998. On the origin and influence of Adèlie Land Bottom Water. In: Jacobs, S.S., Weiss, R.F. (Eds.), Ocean, Ice, and Atmosphere: Interactions at the Antarctic continental margin. . Antarctic Res. Ser., vol. 75. AGU, Washington, pp. 151–171.

Robertson, R., 2005. Baroclinic and barotropic tides in the Ross Sea. Antarct. Sci. 17 (1), 107–120.

Robertson, R., Padman, L., Egbert, G., 1998. Tides in the Weddell Sea. In: Jacobs, S.S., Weiss, R.F. (Eds.), Ocean, Ice, and Atmosphere: Interactions at the Antarctic continental margin. . Antarctic Res. Ser., vol. 75. AGU, Washington, pp. 341–369.

Rohr, J.J., Itsweire, E.C., Helland, K.N., Van Atta, C.W., 1988. Growth and decay of turbulence in a stably stratified shear flow. J. Fluid Mech. 195, 77–111.

Thorpe, S.A., 1977. Turbulence and mixing in a Scottish Loch. Philos. Trans. R. Soc. Lond. Ser. A: Math. Phys. Sci., 286, 125–181.

Visbeck, M., Thurnherr, A., 2008. High-resolution velocity observations of the Drygalski Trough Gravity Plume. Deep-Sea Res. II 55.

Whitworth III, T., Orsi, A., 2006. Antarctic Bottom Water production and export by tides in the Ross Sea. Geophys. Res. Lett. 33, L12609. doi:10.1029/2006GL026357.

Whitworth III, T., Orsi, A.H., Kim, S.-J., Nowlin Jr., W.D., 1998. Water masses and mixing near the Antarctic Slope Front. In: Jacobs, S.S., Weiss, R.F. (Eds.), Ocean, Ice, and Atmosphere: Interactions at the Antarctic continental margin. . Antarct. Res. Ser., vol. 75. AGU, Washington, pp. 1–27.

Williams, G.D., Bindoff, N.L., Marsland, S.J., Rintoul, S.R., 2008. Formation and export of dense shelf water from the Adélie Depression. J. Geophys. Res. 113, C04039. doi:10.1029/2007JC004346.